Supplementary Information

Structural Insights and *In Vitro* and *In Vivo* Anticancer Evaluation of Dithiocarbamate-Based Metal Complexes against Murine Lymphoma

Anupam Singh[a], Riya Patel[a], Samrat Daripa[b], M. K. Bharty[a], R. J. Butcher[c], Sumit Kumar Hira[b*] and Lal Bahadur Prasad[a*]

[a]Department of Chemistry, Institute of Science, Banaras Hindu University, Varanasi 221005, India

[b]Cellular Immunology Laboratory, Department of Zoology, University of Burdwan, Bardhaman 713104, India

[c]Department of Chemistry, Howard University, 525 College Street NW, Washington DC 20059, USA

*Corresponding authors' Email: lbprasad@bhu.ac.in (L. B. Prasad), sumit.hira2008@gmail.com (S. K. Hira)

S.N.	Contents	Page No.
1	FT-IR Spectra	2-8
2	NMR Spectra	8-26
3	Magnetic moment and electronic spectral studies	27-30
4	Mass spectra	30-36
5	Stability and Thermogravimetric Analysis	36-39
6	X-Ray Crystallography	39-50
7	Biological Application	51
8	References	52

1. FT-IR Spectra:

Dithiocarbamate complexes typically exhibit three characteristic absorption bands in their IR spectra: ν(C=S), ν(C–N), and ν(C=N). The IR spectra of ligands **1**–**3** display ν(C=S) stretching vibrations within the range of 1000–1010 cm^{-1} and ν(C–N) vibrations between 1218–1245 cm^{-1}. Upon complexation with metal ions, these bands shift to higher frequencies, with ν(C=S) appearing at 1010–1021 cm^{-1} and ν(C–N) at 1234–1276 cm^{-1}. The notable increase in ν(C–N) frequency in the metal complexes compared to the free ligands suggests π-electron delocalization involving the nitrogen lone pair across the -NCS_2 backbone. Additionally, intense absorption bands observed between 1490–1514 cm^{-1} correspond to ν(C=N) vibrations, indicating partial C=N character associated with the thioureide moiety. The IR spectra of ligands and their corresponding metal complexes are illustrated in Figures S1–S12.

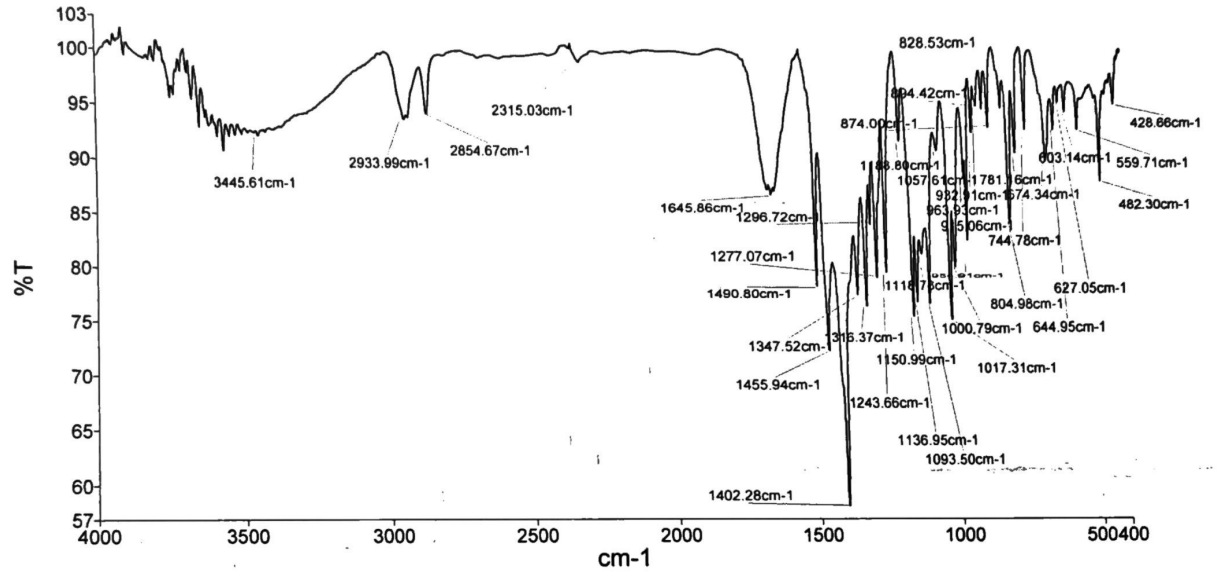

Figure S1. FT-IR spectrum of ligand **1**.

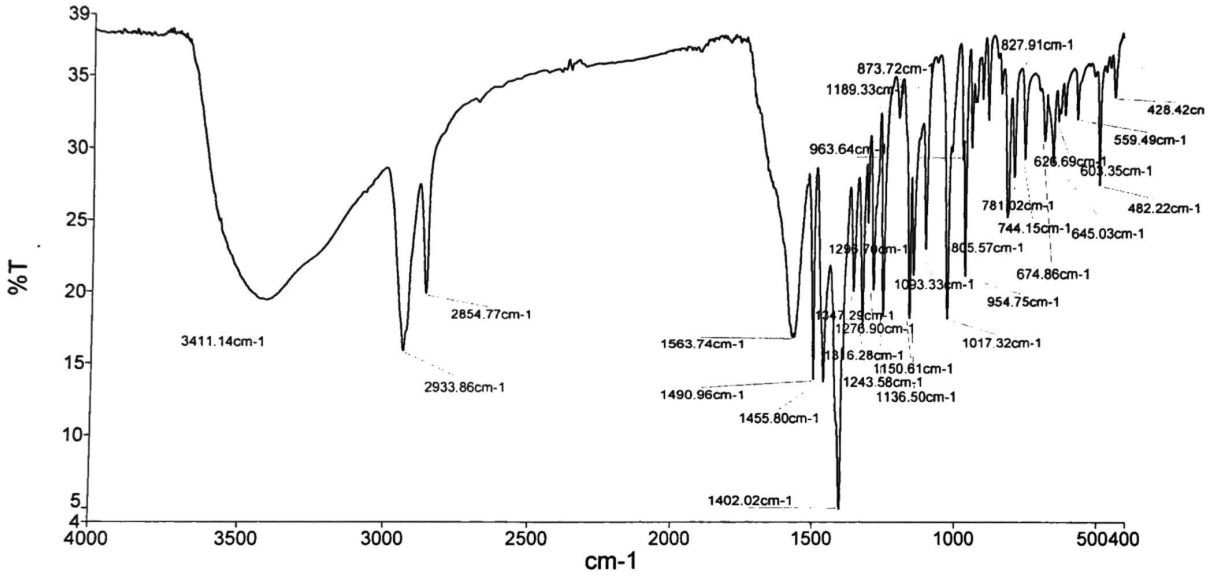

Figure S2. FT-IR spectrum of complex **1a**.

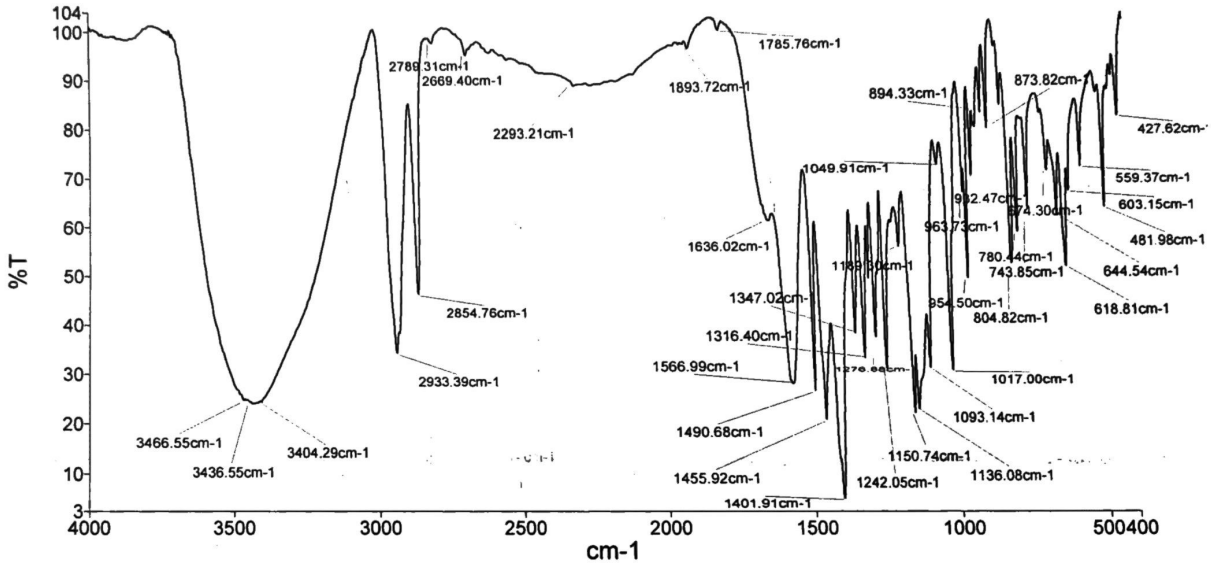

Figure S3. FT-IR spectrum of complex **1b**.

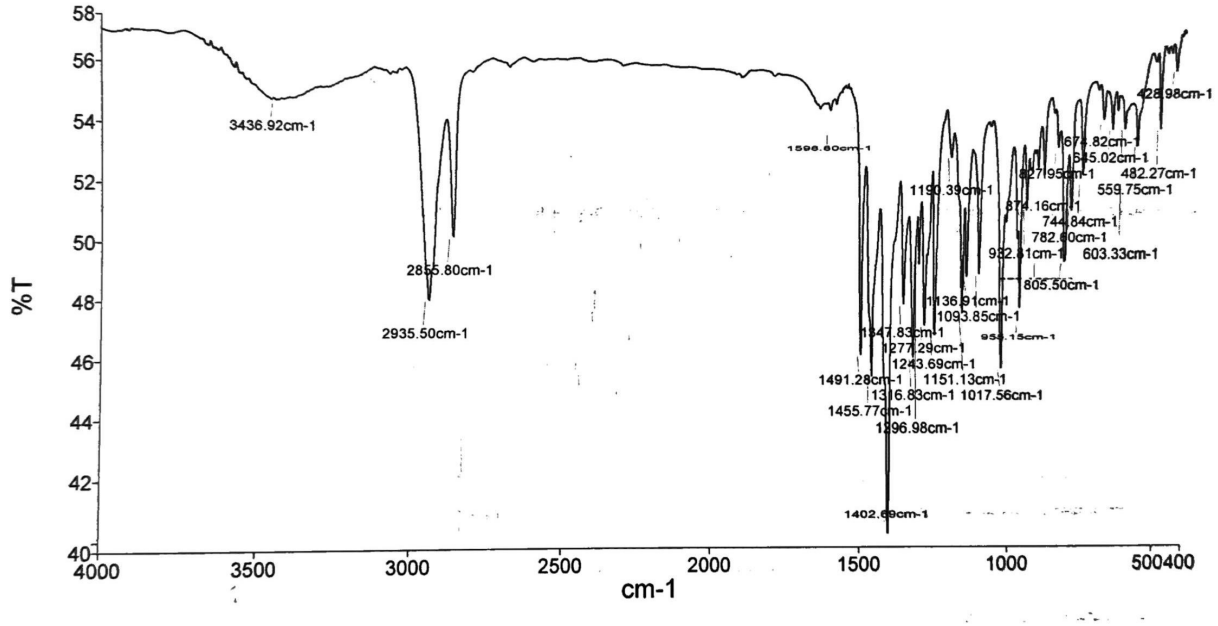

Figure S4. FT-IR spectrum of complex **1c**.

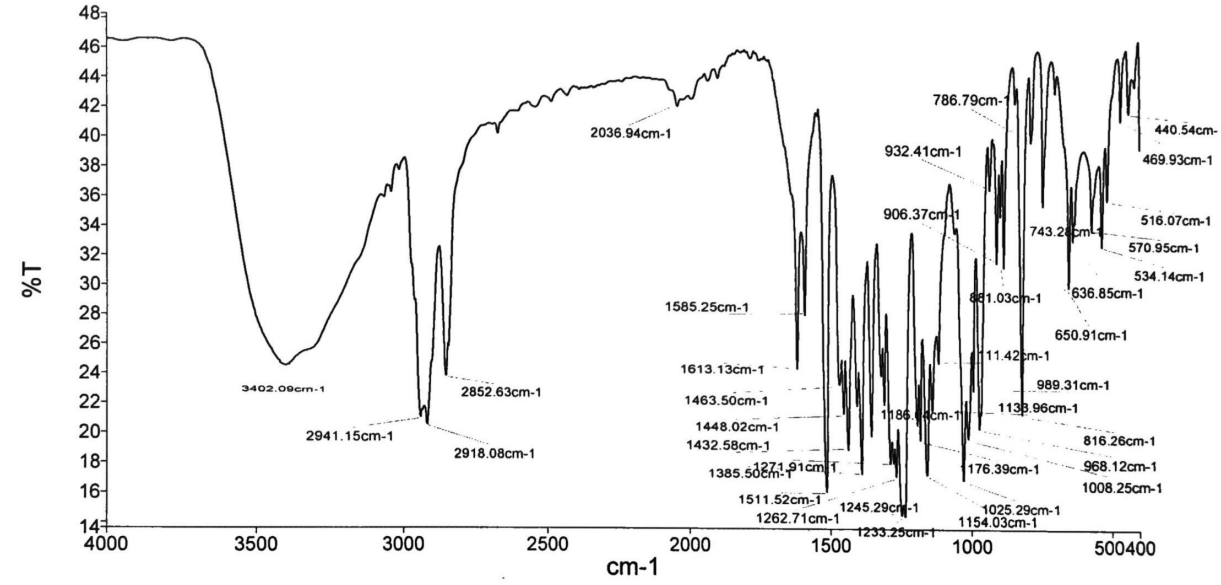

Figure S5. FT-IR spectrum of ligand **2**.

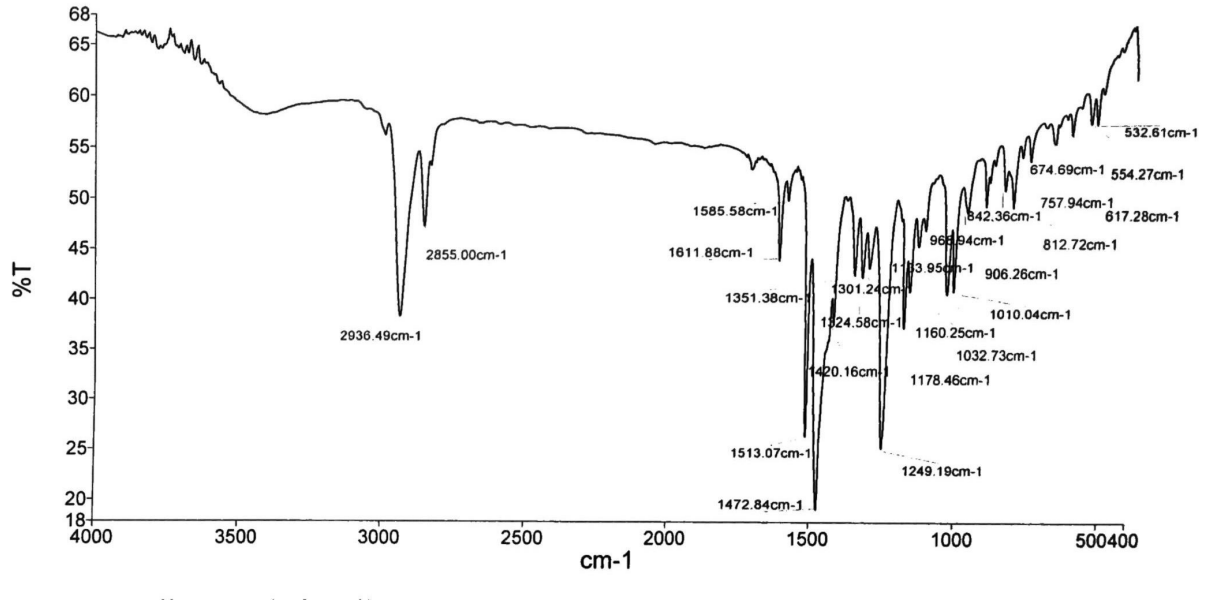

Figure S6. FT-IR spectrum of complex **2a**.

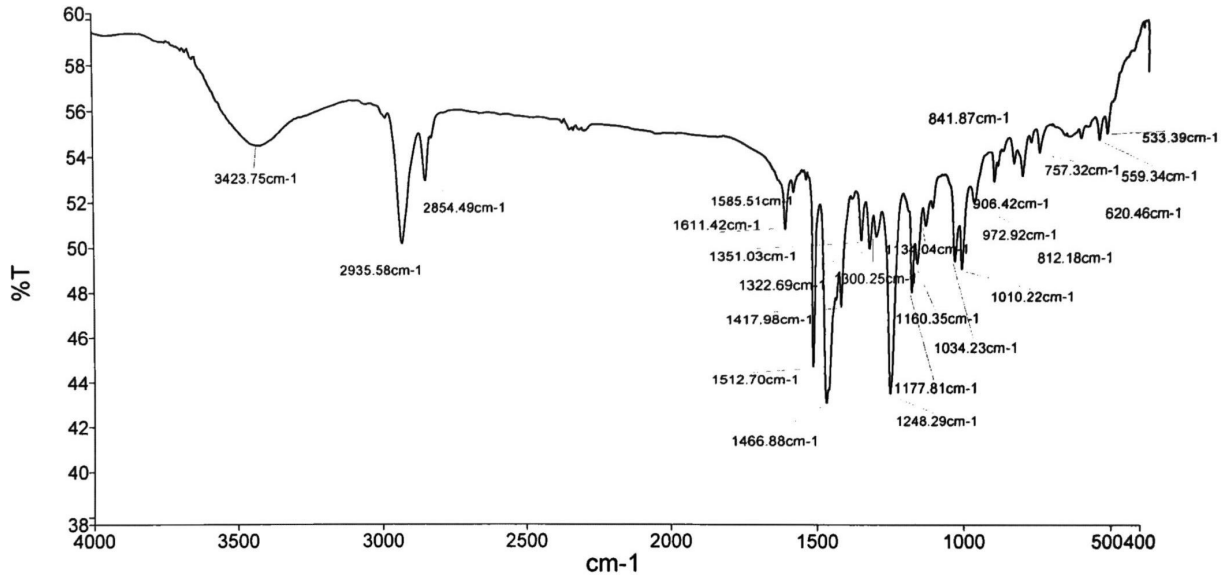

Figure S7. FT-IR spectrum of complex **2b**.

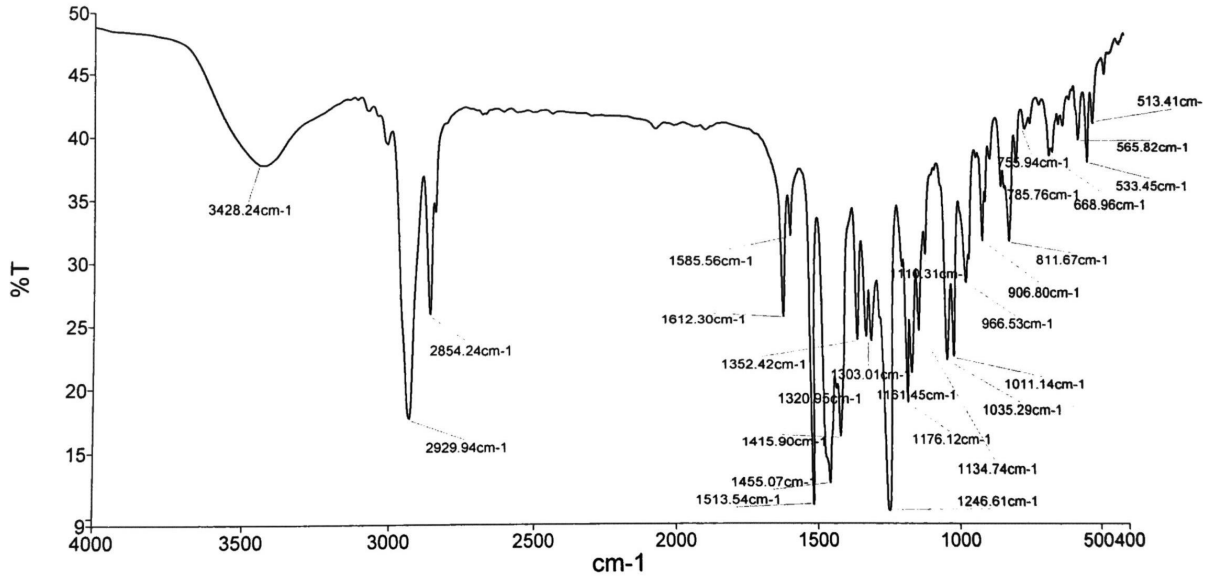

Figure S8. FT-IR spectrum of complex **2c**.

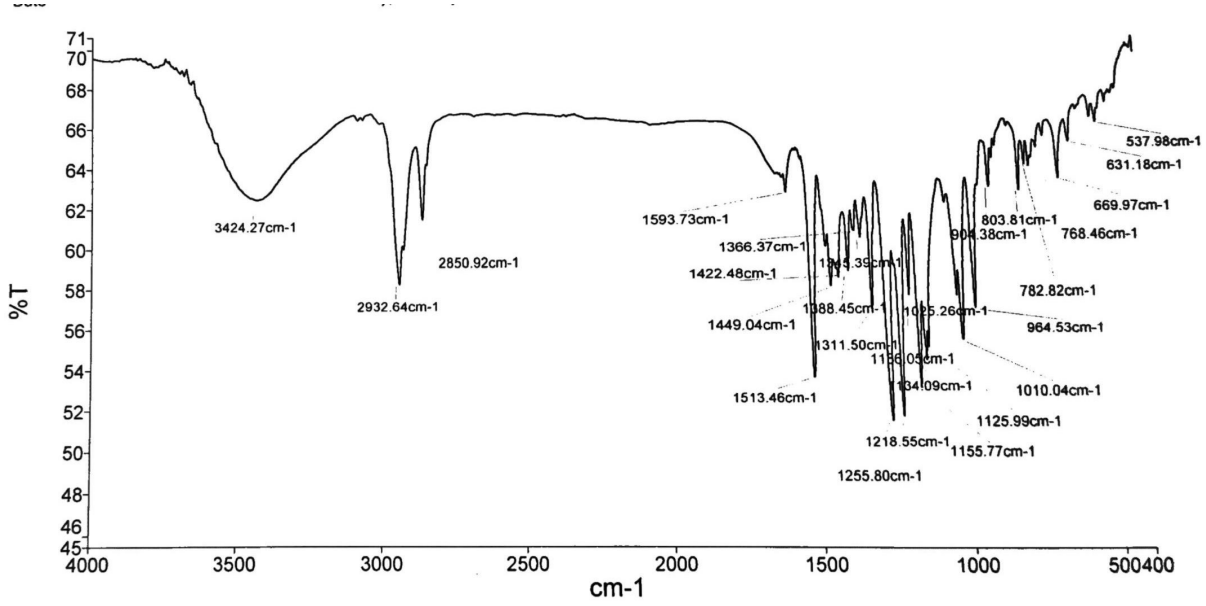

Figure S9. FT-IR spectrum of ligand **3**.

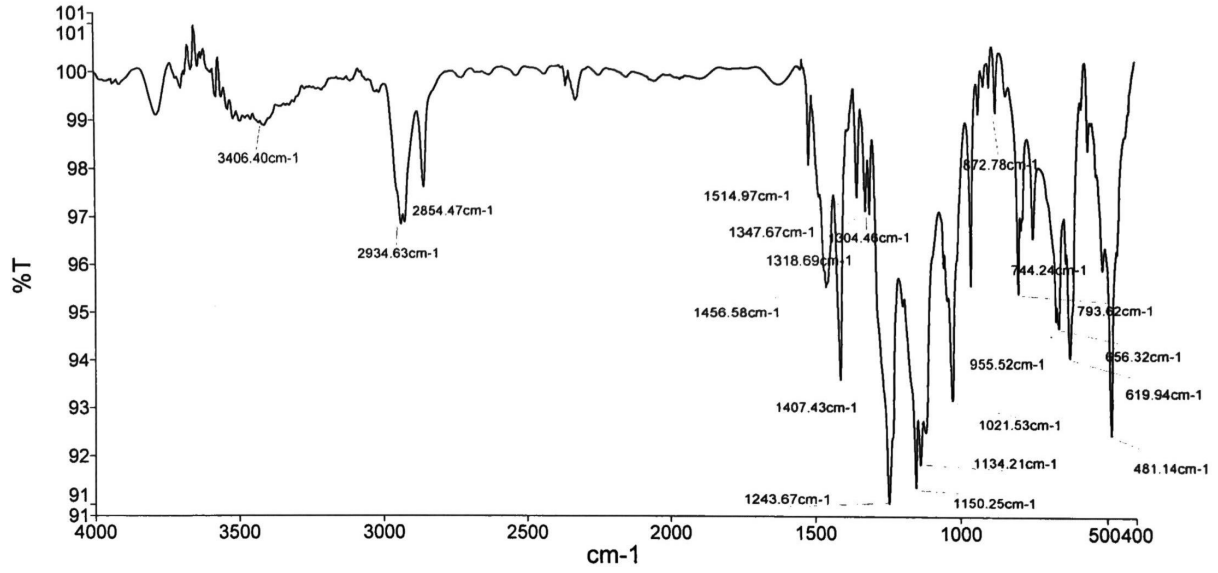

Figure S10. FT-IR spectrum of complex **3a**.

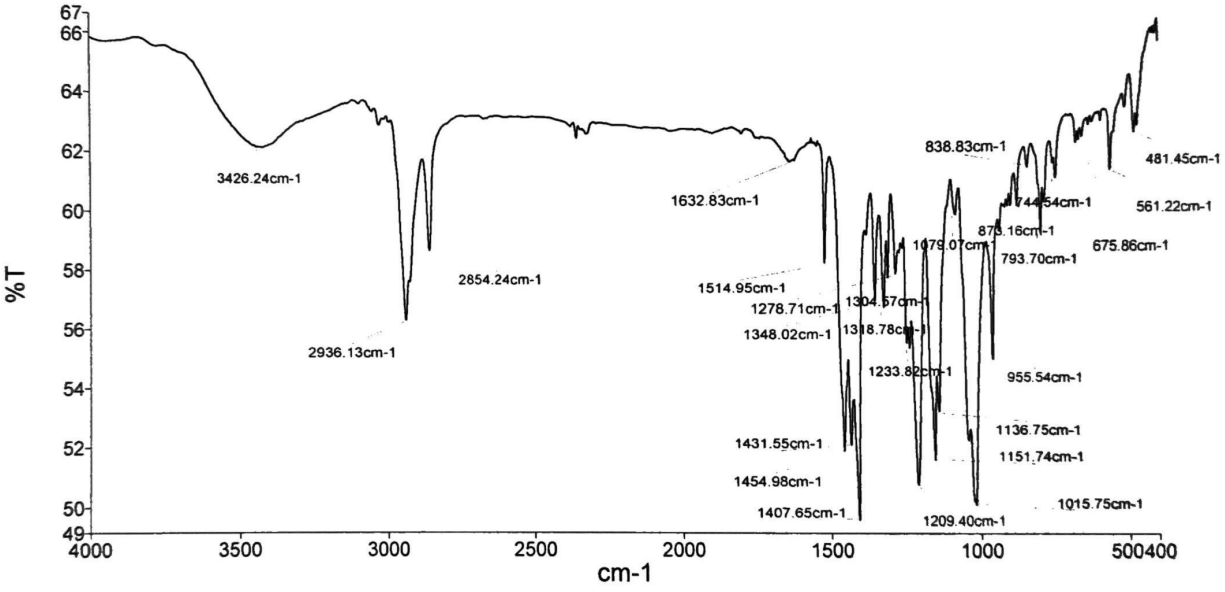

Figure S11. FT-IR spectrum of complex **3b**.

Figure S12. FT-IR spectrum of complex **3c**.

2. NMR Spectra:

The NMR spectra of the ligands **1-3** and their metal complexes were recorded in the $CDCl_3$/DMSO-d_6 and the resulting spectra are given in Figures S13-S30. In the ^1H NMR spectra of the ligands **1-3**, signals for aromatic protons were observed in the range of δ 7.26-7.22, 7.19-6.75, and 7.13-6.99 ppm respectively. The aromatic protons signals in the spectra of complexes **1a**, **1c**, **2a**, **2c**, **3a**, and **3c** were observed in the range of δ 7.48-7.20, 6.85-6.77, 7.81-7.76, 6.45-6.05, 6.98-6.90, and 7.14-7.09 ppm respectively. After complexation, the δ values of aromatic protons showed no significant changes, suggesting that the aromatic ring did not interact with metal ions. Sharp singlet signals appeared at δ 5.32, 5.31 and 5.33 ppm in spectra of ligands **1-3** due to methylene protons attached with 4-chlorophenyl, 4-methoxyphenyl and 4-methylphenyl rings respectively. However, the signals for the same methylene protons in the metal complexes **1a**, **1c**, **2a**, **2c**, **3a**, and **3c** were observed at δ 4.13, 4.32, 5.32, 4.28, 5.36, and 5.49 ppm respectively. Cyclohexyl protons were observed in the aliphatic region.

^{13}C NMR spectrum of the ligands **1-3** showed a signal at δ 215.78, 215.74, and 215.20 ppm respectively due to the carbon present in -NCS_2 moiety, while the signal for the same carbon was observed at δ 206.59, 208.97, 208.42, 204.79, 197.85, and 197.73 in the ^{13}C NMR spectra of complexes **1a**, **1c**, **2a**, **2c**, **3a**, and **3c** respectively.

After complexation, an up-field shift was observed in the δ values of the C=S carbon within the -NCS_2 moiety, indicating the formation of a metal-sulfur bond. The signals for the aromatic ring's carbons were observed in the range of δ 140.87-127.77, 157.78-113.29, and 138.28-126.81 ppm in the ligands **1**-**3** respectively, while the signals for the aromatic carbons in their metal complexes were observed in the range of δ 131.82-124.22 (**1a**), 134.22-128.10 (**1c**), 159.09-114.03 (**2a**), 158.86-113.98 (**2c**), 134.14-126.57 (**3a**) and 136.41-126.45 ppm (**3c**) respectively. Methylene carbon attached with aromatic ring resonated at δ 58.21, 49.92, and 57.57 ppm in the ligands **1**-**3** while at δ 48.60, 47.67, 48.32, 52.07, 53.51, and 53.38 ppm in complexes **1a**, **1c**, **2a**, **2c**, **3a** and **3c** respectively. Methoxy carbon present in ligand **2** and its complexes **2a** and **2c** resonated at δ 55.43, 55.35, and 55.43 ppm respectively. Methyl carbon in ligand **3** and its metal complexes **3a** and **3c** showed signals at δ 20.67, 21.23, and 21.11 ppm respectively. However, cyclohexyl carbons showed NMR signals in the aliphatic region. There were no significant changes were noticed in the δ values of the carbons other than -NCS_2 upon complexation which confirmed that they were not involved in metal-ligand coordination.

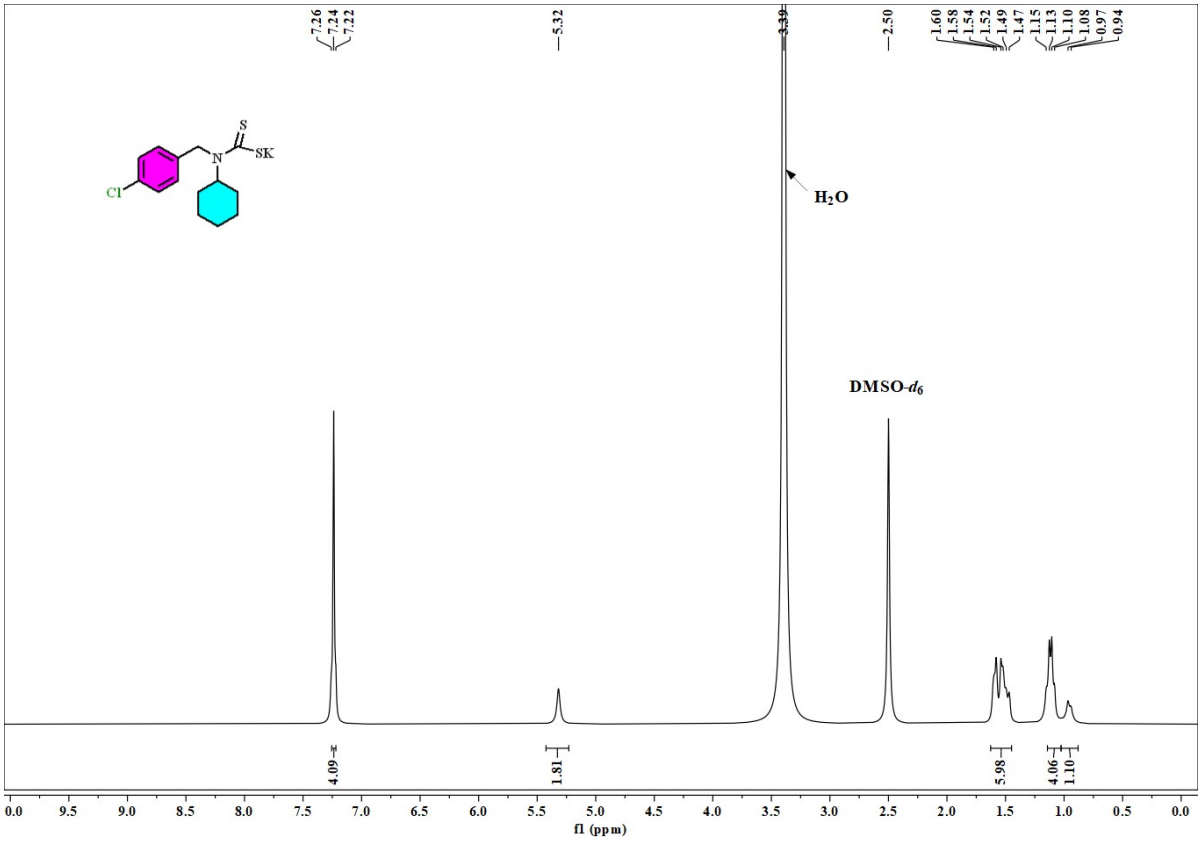

Figure S13. ^{1}H NMR spectrum of ligand **1**. ^{1}H NMR (500 MHz, DMSO-d_6, ppm): δ 7.26-7.22 (m, 4H, aromatic), δ 5.32 (s, 2H, methylene), δ 1.60-0.94 (m, 11H, cyclohexyl ring).

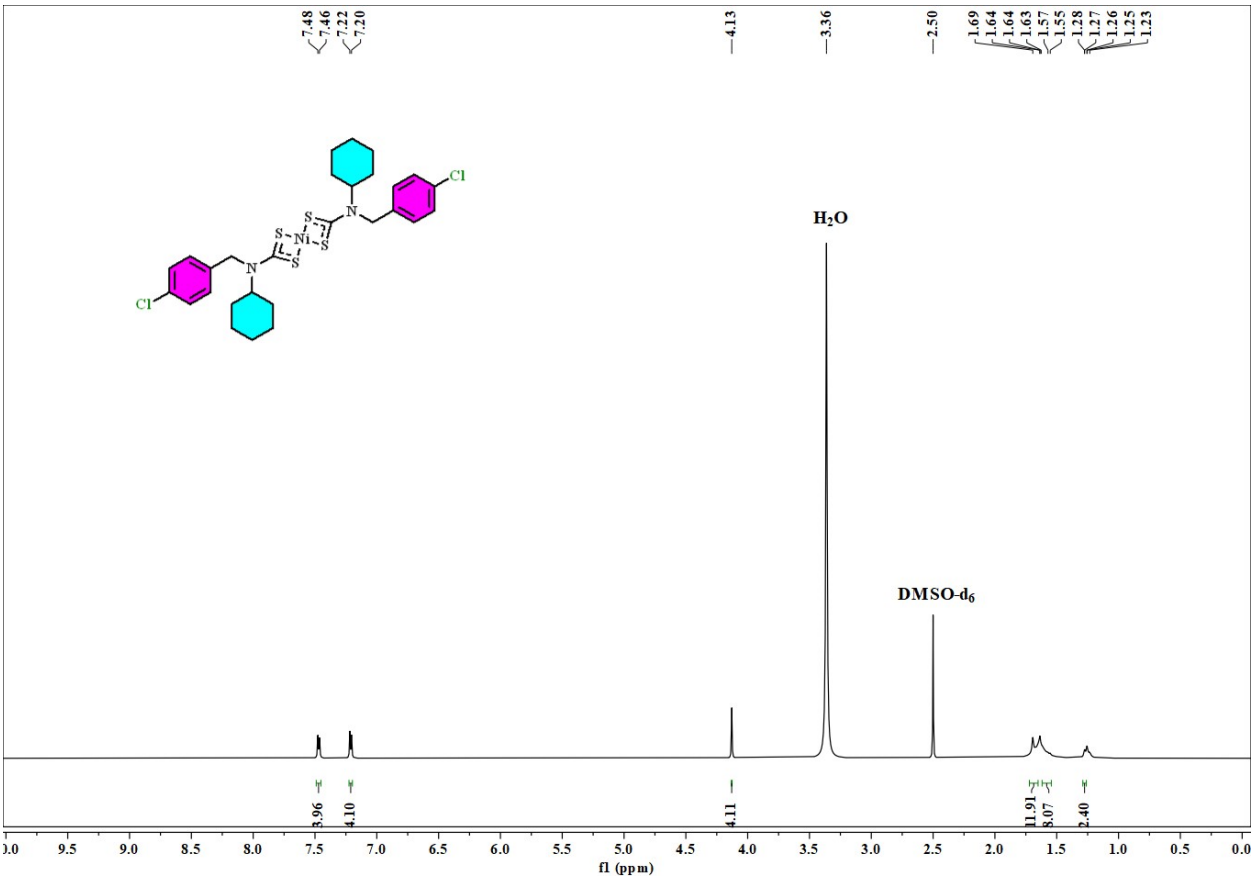

Figure S14. ^{1}H NMR spectrum of complex **1a**. ^{1}H NMR (500 MHz, DMSO-d_6, ppm): δ 7.48, 7.46 (d, 4H, J= 10Hz, aromatic), δ 7.22, 7.20 (d, 4H, J= 10Hz, aromatic), δ 4.13 (s, 4H, methylene), δ 1.69-1.23 (m, 22H, cyclohexyl ring).

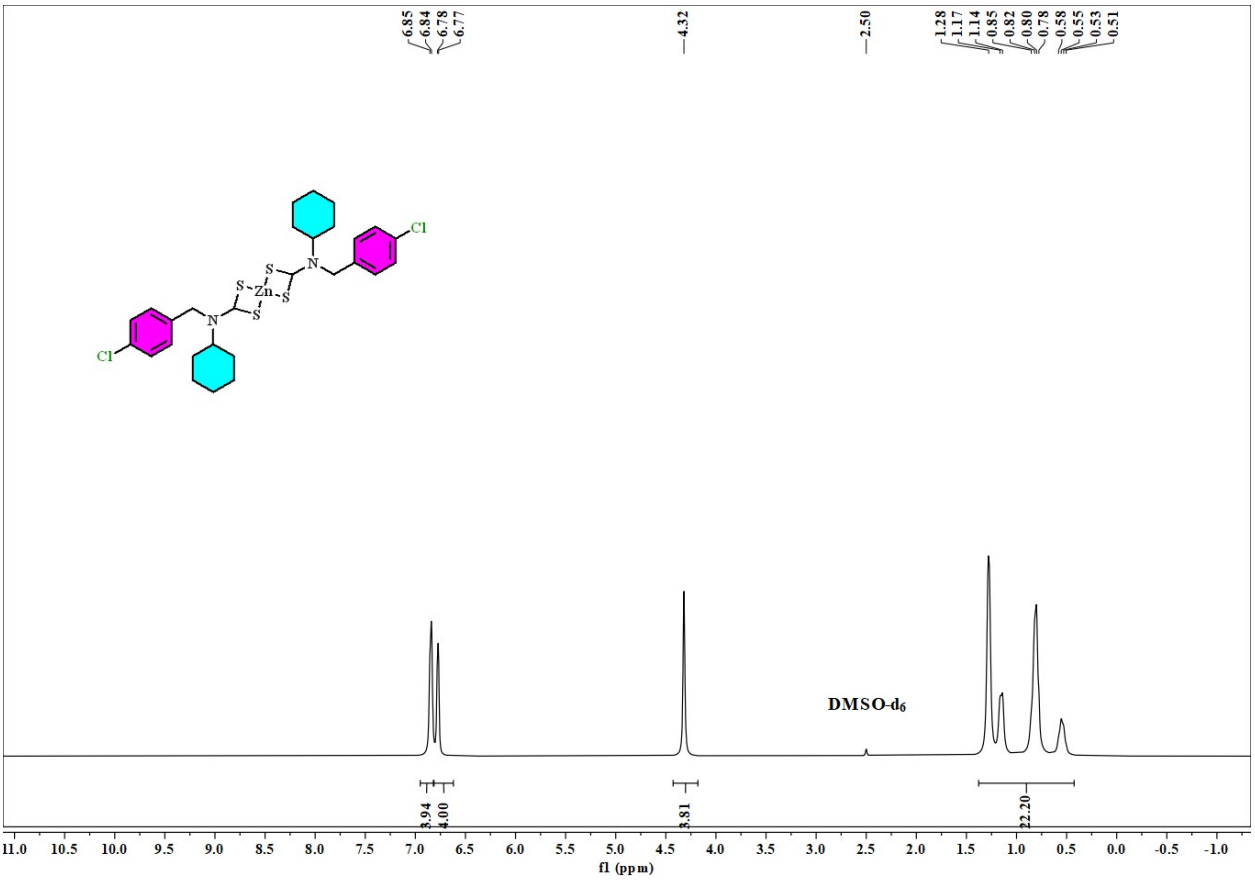

Figure S15. ^{1}H NMR spectrum of complex **1c**. ^{1}H NMR (600 MHz, DMSO-d_6, ppm): δ 6.85-6.84 (d, 4H, J= 6Hz aromatic), δ 6.78-6.77 (d, 4H, J= 6Hz aromatic), δ 4.32 (s, 4H, methylene), δ 1.28-0.51 (m, 22H, cyclohexyl).

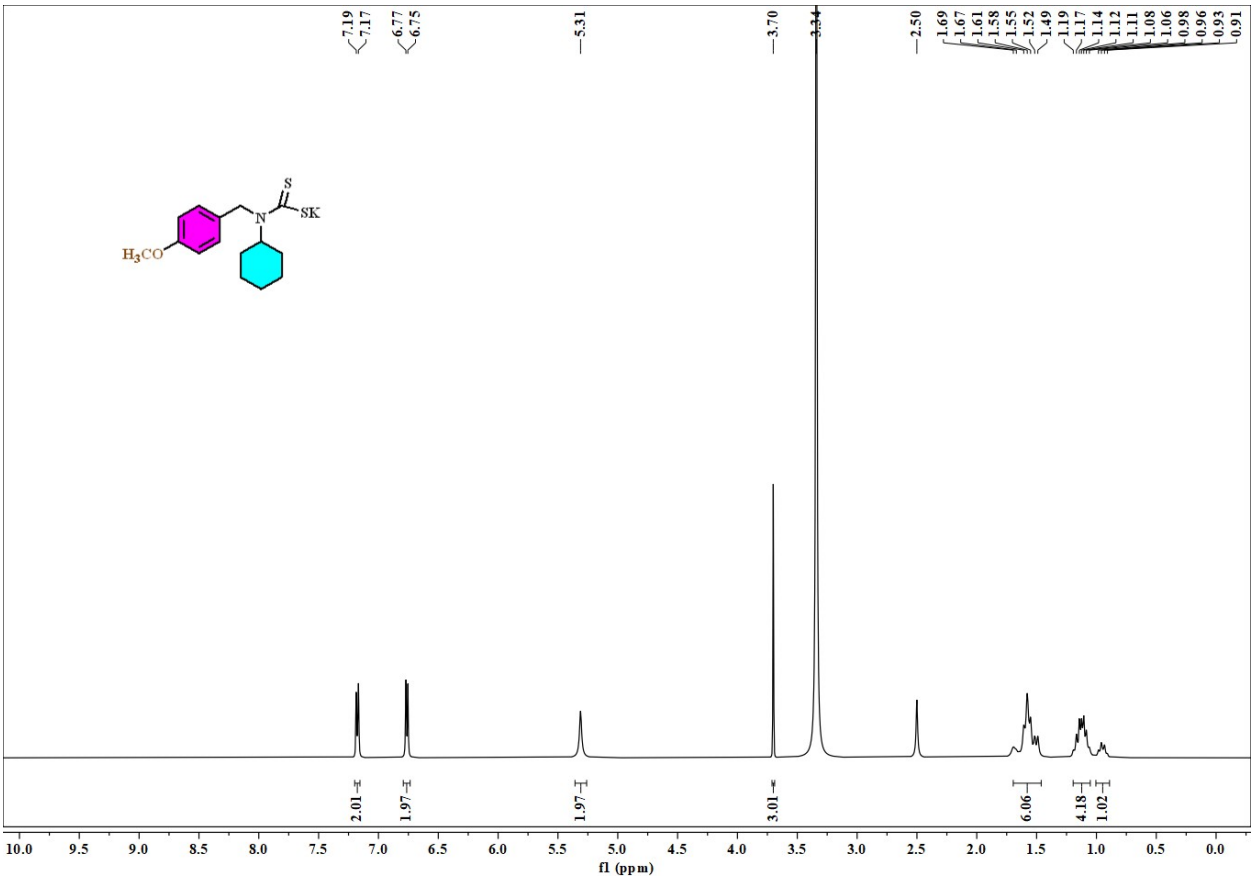

Figure S16. ^{1}H NMR spectrum of ligand **2**. ^{1}H NMR (500 MHz, DMSO-d_6, ppm): δ 7.19,7.17 (d, 2H, J= 10Hz, aromatic), δ 6.77-6.75 (d, 2H, J= 10Hz, aromatic), δ 5.31 (s, 2H, methylene), δ 3.70 (s, 3H, methoxy), δ 1.69-0.91 (m, 11H, cyclohexyl ring).

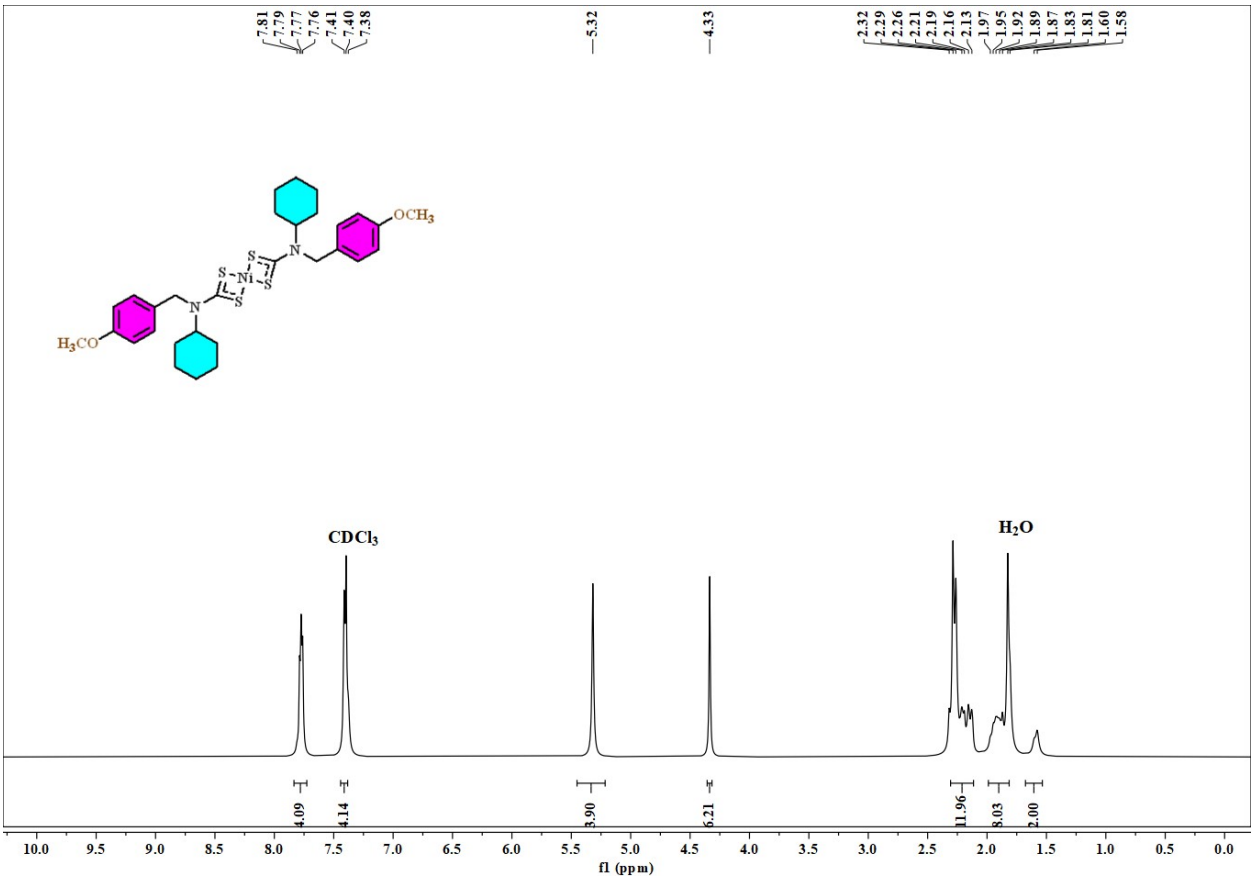

Figure S17. ^{1}H NMR spectrum of complex **2a**. ^{1}H NMR (500 MHz, $CDCl_3$, ppm): δ 7.81,7.79 (d, 4H, J= 10Hz, aromatic), δ 7.77-7.76 (d, 4H, J= 5Hz, aromatic), δ 5.32 (s, 4H, methylene), δ 4.33 (s, 6H, methoxy), δ 2.32-0.1.58 (m, 22H, cyclohexyl ring).

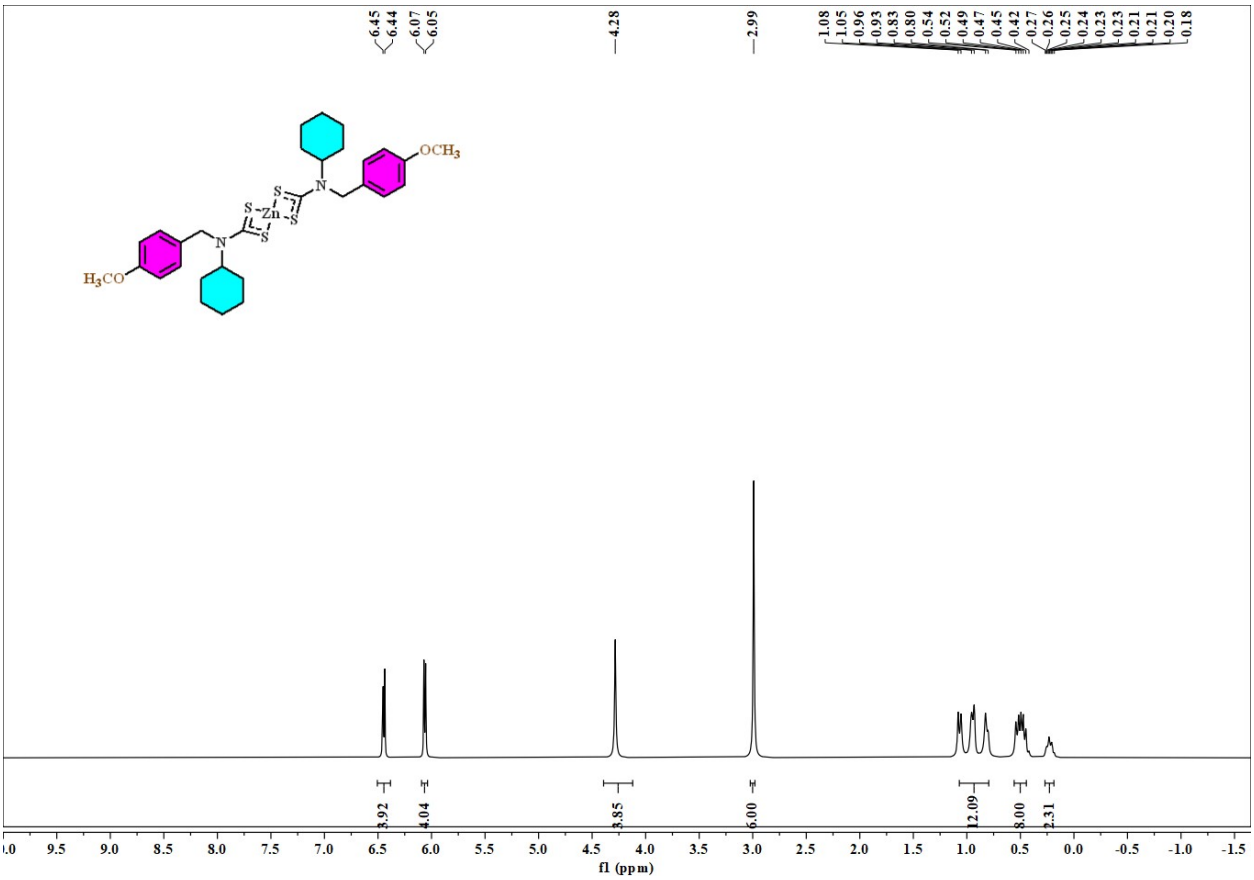

Figure S18. ^{1}H NMR spectrum of complex **2c**. ^{1}H NMR (500 MHz, $CDCl_3$, ppm): δ 6.45,6.44 (d, 4H, J= 5Hz, aromatic), δ 6.07-6.05 (d, 4H, J= 10Hz, aromatic), δ 4.28 (s, 4H, methylene), δ 2.99 (s, 6H, methoxy), δ 1.08-0.18 (m, 22H, cyclohexyl ring).

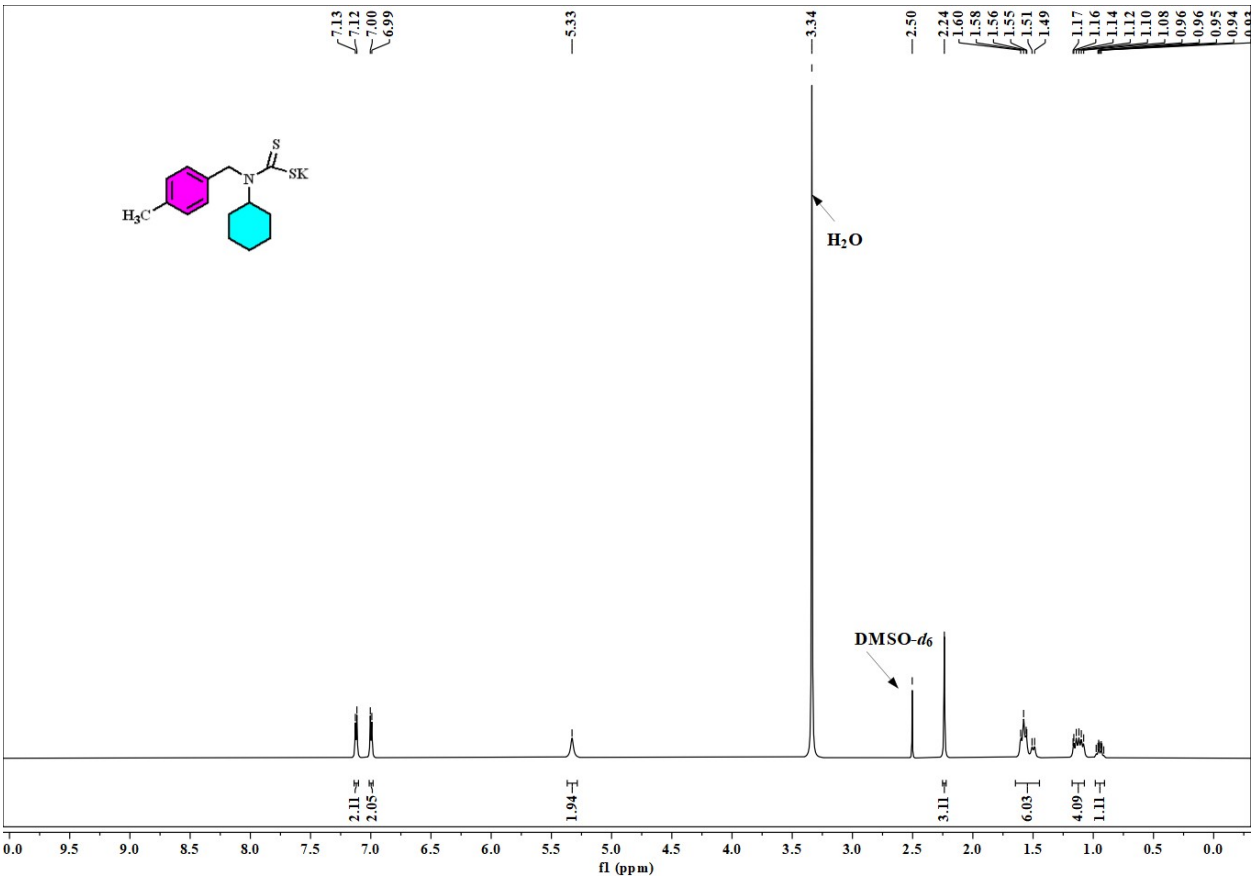

Figure S19. ^{1}H NMR spectrum of ligand **3**. ^{1}H NMR (600 MHz, DMSO-d_6, ppm): δ 7.13,7.12 (d, 2H, J= 6Hz, aromatic), δ 7.00-6.99 (d, 2H, J= 6Hz, aromatic), δ 5.33 (s, 2H, methylene), δ 2.24 (s, 3H, methyl), δ 1.60-0.93 (m, 11H, cyclohexyl ring).

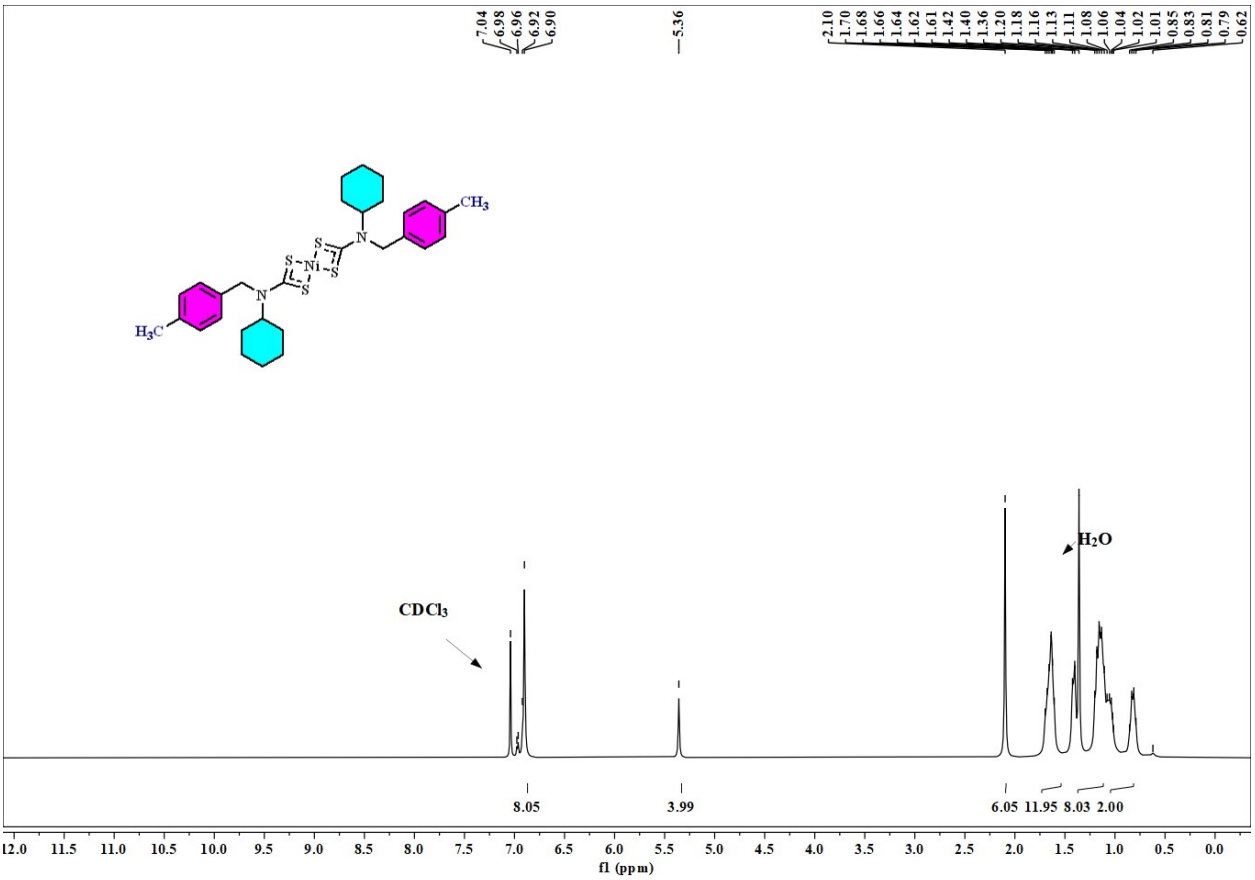

Figure S20. ^{1}H NMR spectrum of complex **3a**. ^{1}H NMR (600 MHz, $CDCl_3$, ppm): δ 6.98-6.90 (m, 8H, aromatic), δ 5.36 (s, 4H, methylene), δ 2.10 (s, 6H, methyl), δ 1.70-0.62 (m, 22H, cyclohexyl ring).

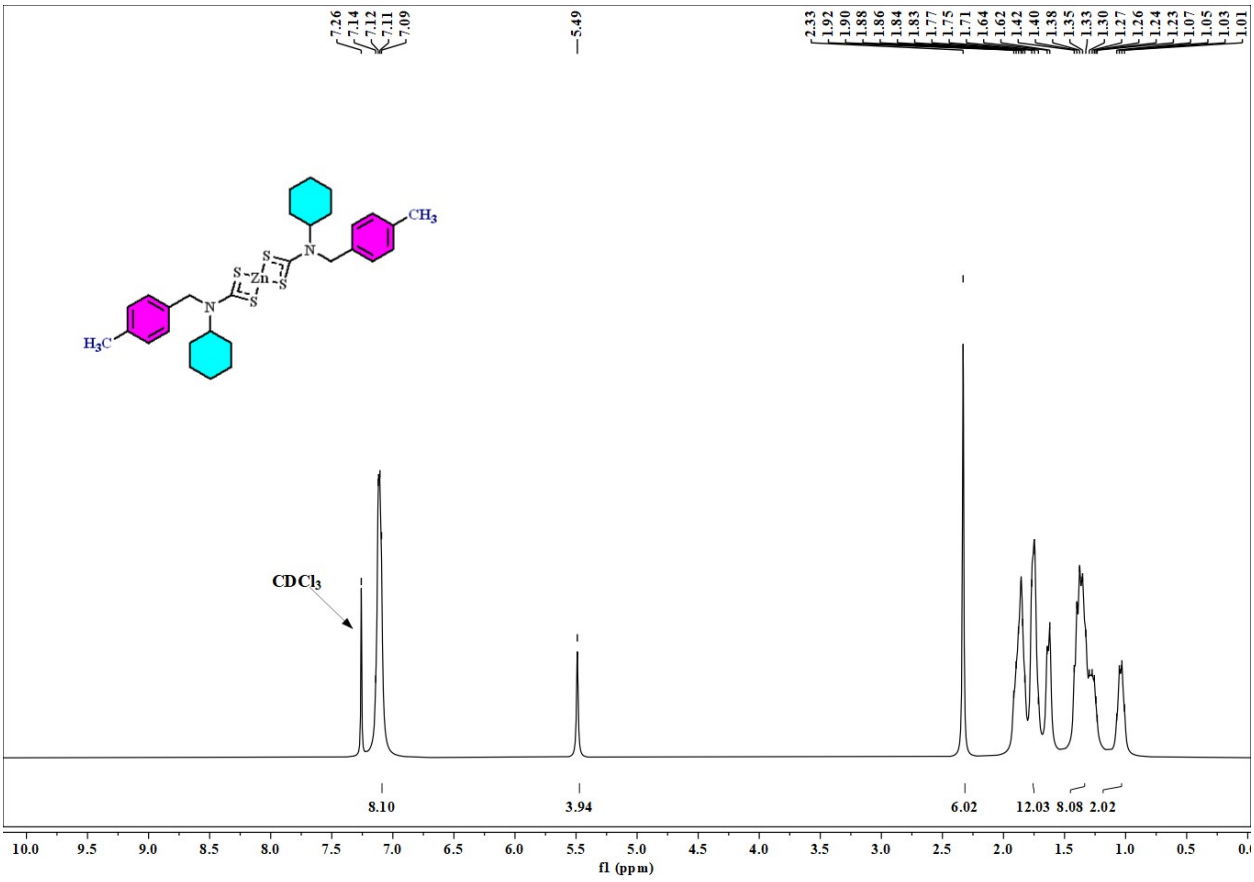

Figure S21. ^{1}H NMR spectrum of complex **3c**. ^{1}H NMR (600 MHz, $CDCl_3$, ppm): δ 7.14-7.09 (m, 8H, aromatic), δ 5.49 (s, 4H, methylene), δ 2.33 (s, 6H, methyl), δ 1.92-1.01 (m, 22H, cyclohexyl ring).

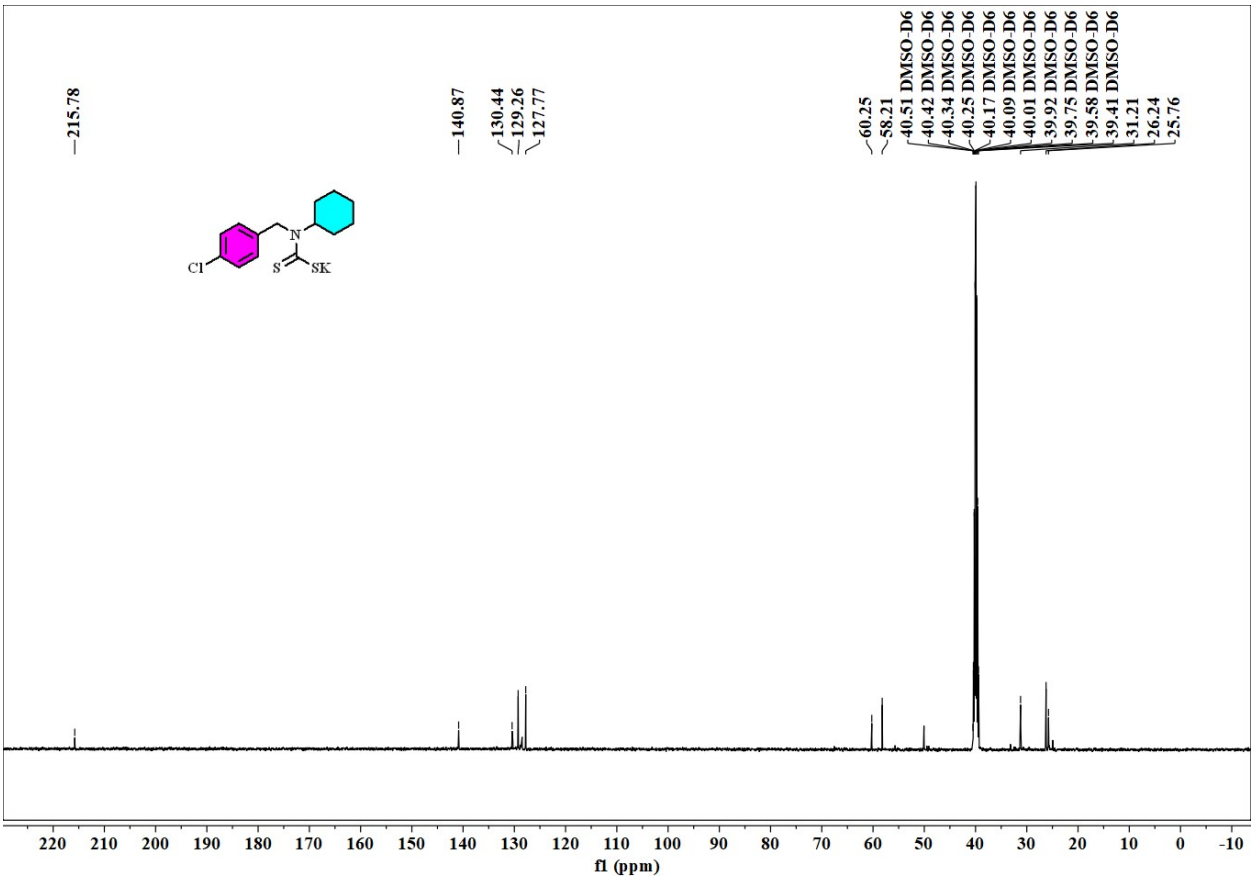

Figure S22. ^{13}C NMR spectrum of ligand **1**. $^{13}C\{^{1}H\}$ NMR (125 MHz, DMSO-d_6, ppm): δ 215.78 ($-CS_2$), δ 140.87, 130.44, 129.26, 127.77 (aromatic carbons), δ 58.21 (methylene), δ 60.25, 31.21, 26.24, 25.76 (cyclohexyl ring carbons).

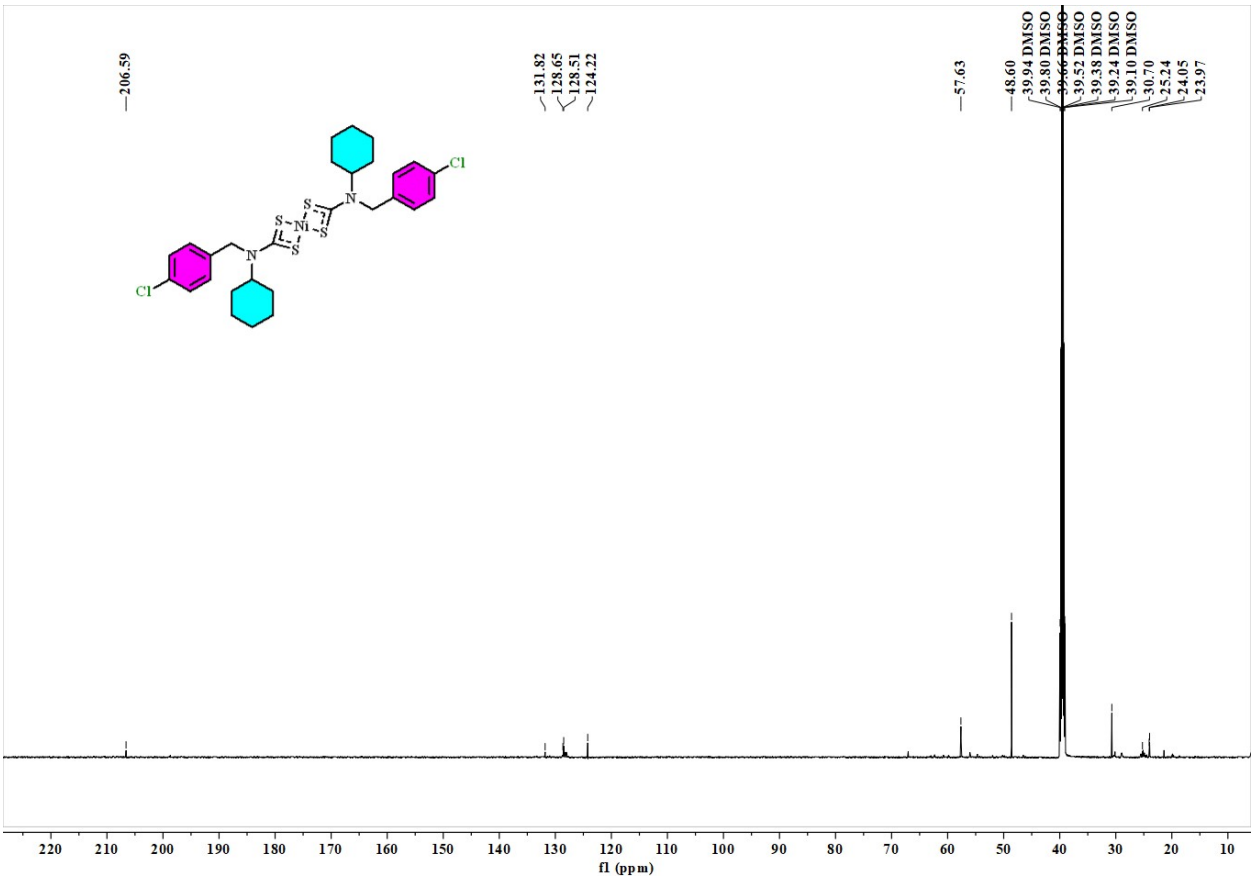

Figure S23. ^{13}C NMR spectrum of complex **1a**. $^{13}C\{^{1}H\}$ NMR (125 MHz, DMSO-d_6, ppm): δ 206.59 (-CS_2), δ 131.82, 128.65, 128.51, 124.22 (aromatic carbons), δ 48.60 (methylene), δ 57.63, 30.70, 25.24, 23.97 (cyclohexyl ring carbons).

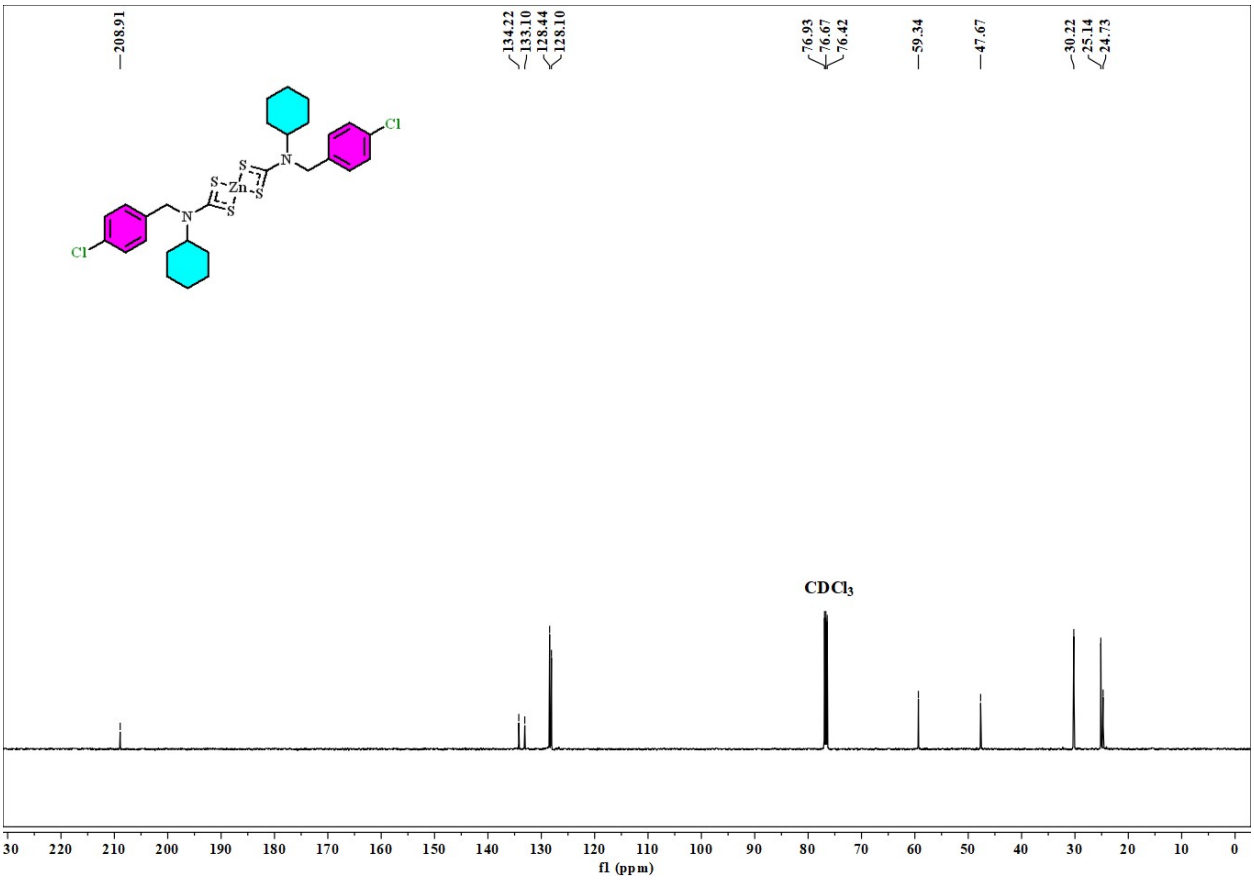

Figure S24. ^{13}C NMR spectrum of complex **1c**. $^{13}C\{^{1}H\}$ NMR (150 MHz, $CDCl_3$, ppm): δ 208.91 ($-CS_2$), δ 134.22, 133.10, 128.44, 128.10 (aromatic), δ 47.67 (methylene), δ 59.34, 30.22, 25.14, 24.73 (cyclohexyl).

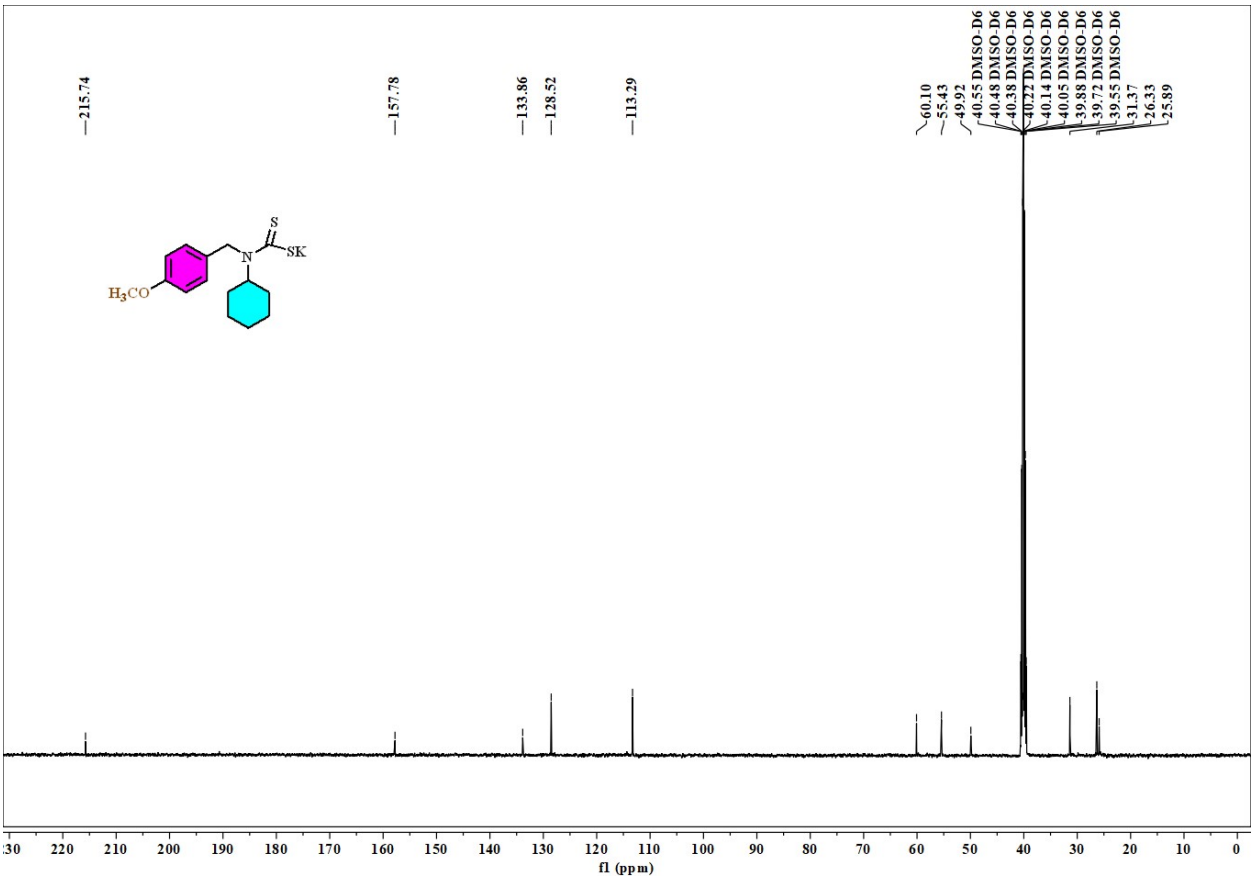

Figure S25. ^{13}C NMR spectrum of ligand **2**. $^{13}C\{^{1}H\}$ NMR (125 MHz, DMSO-d_6, ppm): δ 215.74 (-CS_2), δ 157.78, 133.86, 128.52, 113.29 (aromatic carbons), δ 55.43 (methoxy), δ 49.92 (methylene), δ 60.10, 31.37, 26.33, 25.89 (cyclohexyl ring carbons).

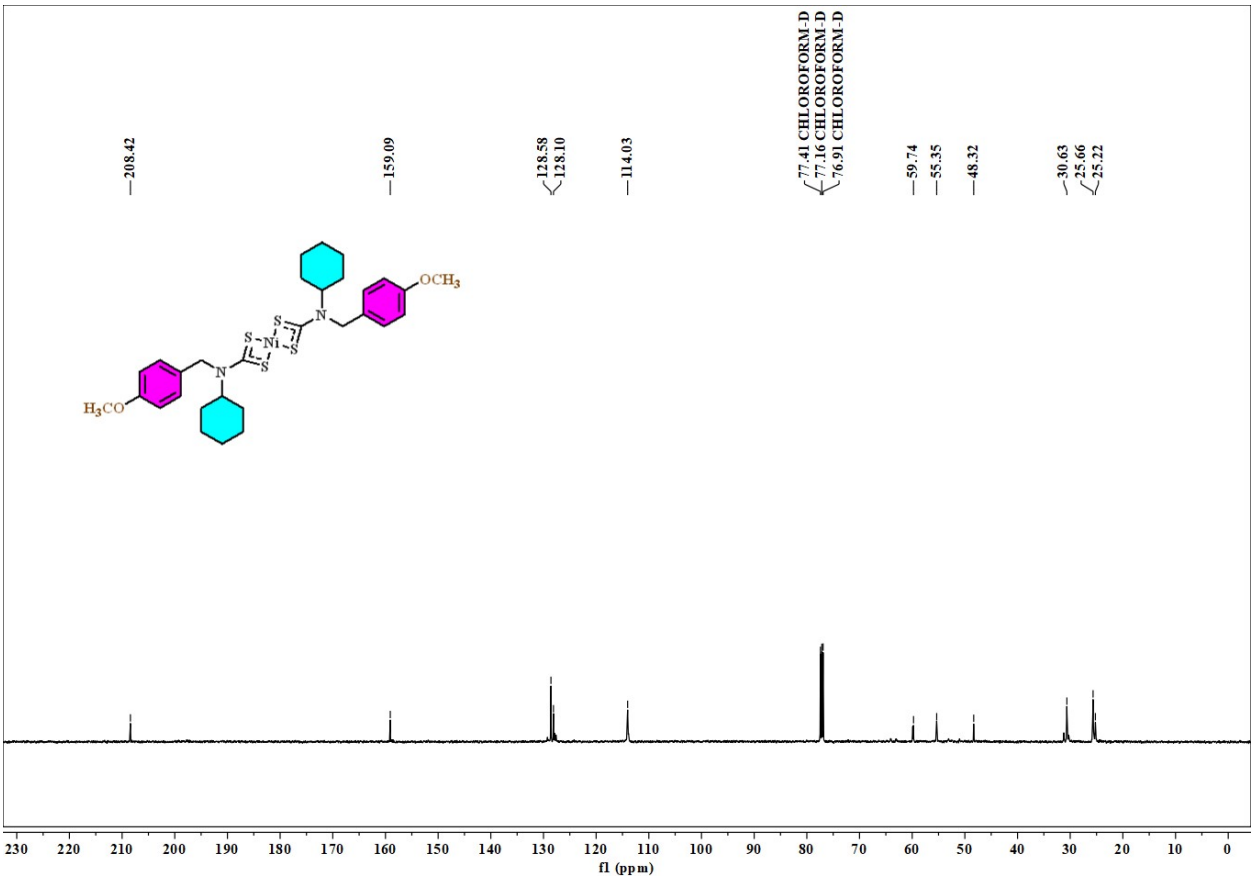

Figure S26. ^{13}C NMR spectrum of complex **2a**. $^{13}C\{^{1}H\}$ NMR (125 MHz, $CDCl_3$, ppm): δ 208.42 ($-CS_2$), δ 159.09, 128.58, 128.10, 114.03 (aromatic carbons), δ 55.35 (methoxy), δ 48.32 (methylene), δ 59.74, 30.63, 25.66, 25.22 (cyclohexyl ring carbons).

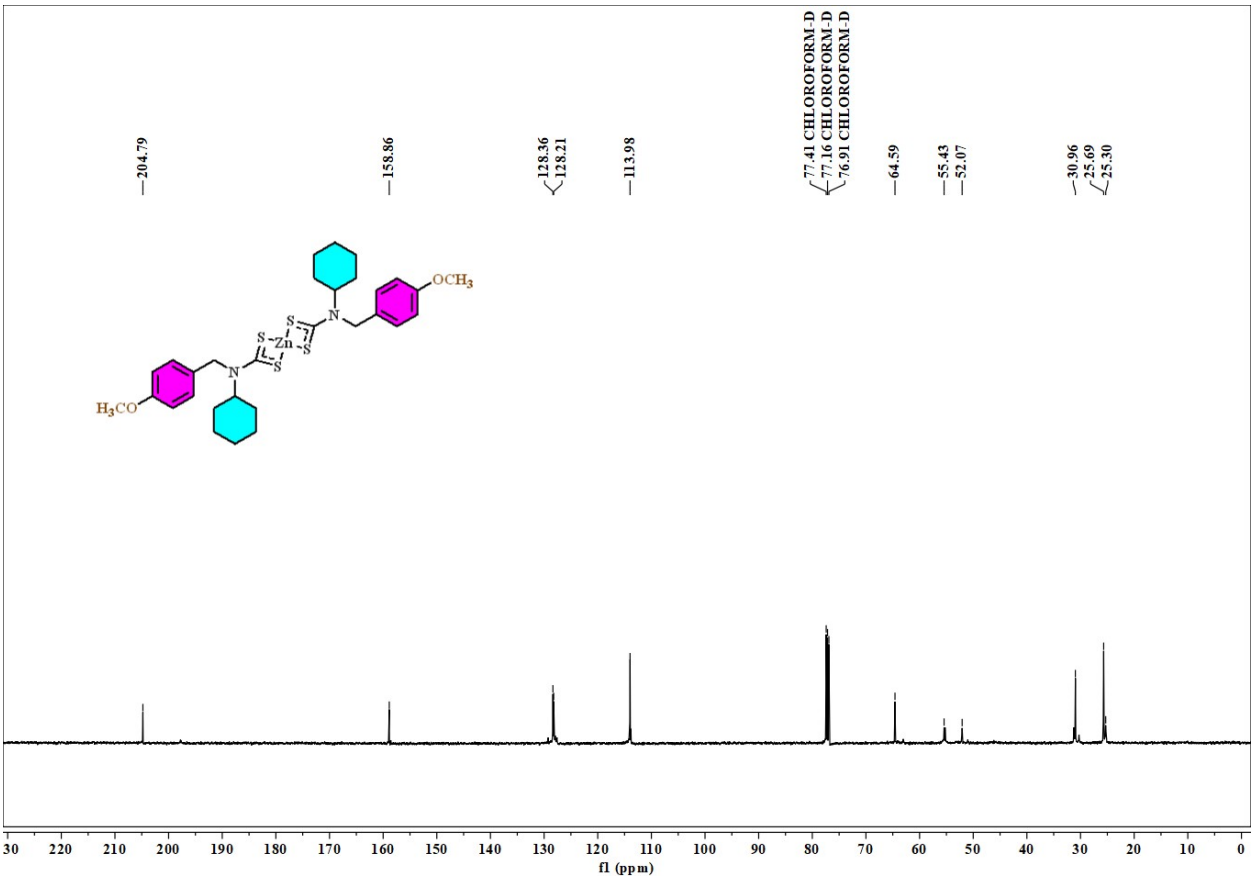

Figure S27. ^{13}C NMR spectrum of complex **2c**. $^{13}C\{^{1}H\}$ NMR (125 MHz, $CDCl_3$, ppm): δ 204.79 ($-CS_2$), δ 158.86, 128.36, 128.21, 113.98 (aromatic carbons), δ 55.43 (methoxy), δ 52.07 (methylene), δ 64.59, 30.96, 25.69, 25.30 (cyclohexyl ring carbons).

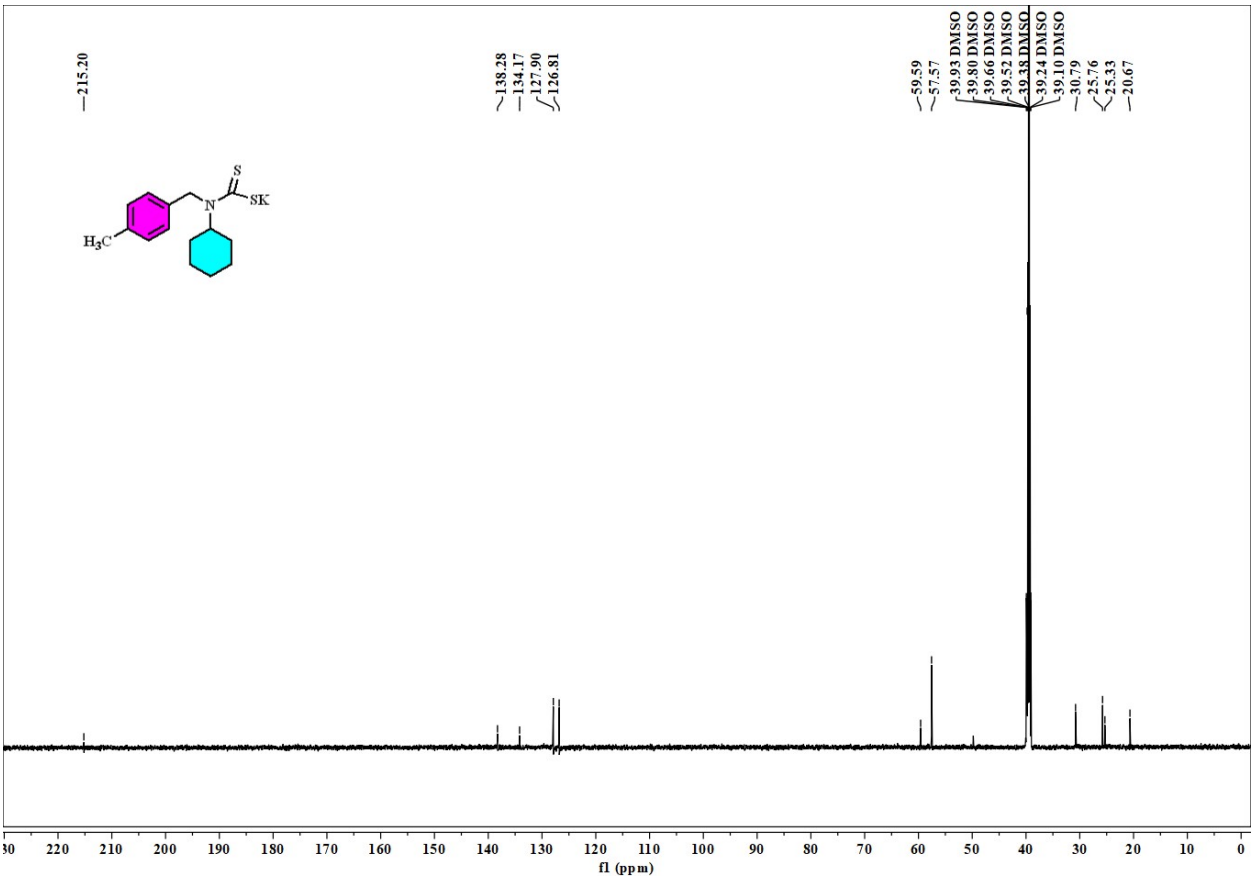

Figure S28. ^{13}C NMR spectrum of ligand **3**. $^{13}C\{^{1}H\}$ NMR (150 MHz, DMSO-d_6, ppm): δ 215.20 (-CS_2), δ 138.28, 134.17, 127.90, 126.81 (aromatic carbons), δ 57.57 (methylene), δ 59.59, 30.79, 25.76, 25.33 (cyclohexyl ring carbons) δ 20.67 (methyl carbon).

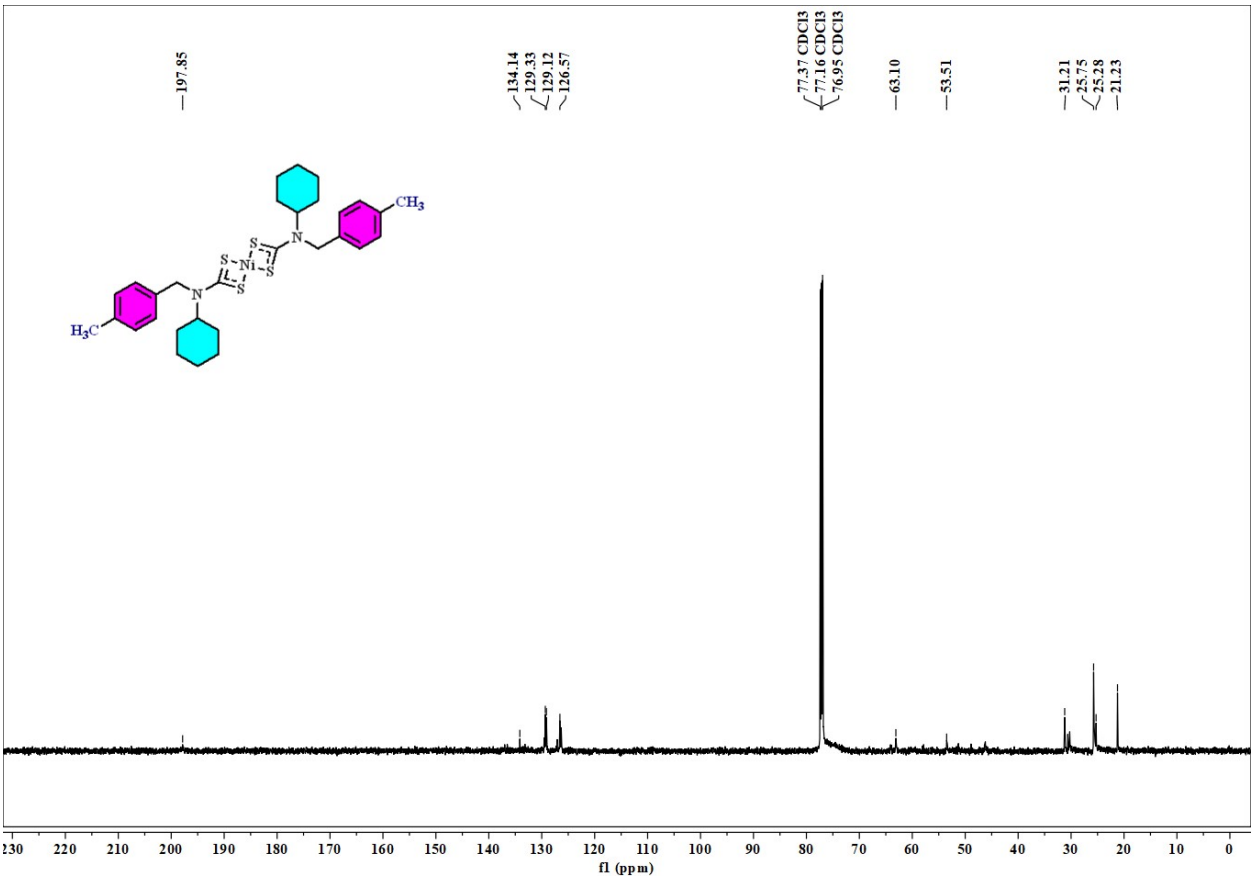

Figure S29. ^{13}C NMR spectrum of complex **3a**. $^{13}C\{^{1}H\}$ NMR (150 MHz, $CDCl_3$, ppm): δ 197.85 ($-CS_2$), δ 134.14, 129.33, 129.12, 126.57 (aromatic carbons), δ 53.51 (methylene), δ 63.10, 31.21, 25.75, 25.28 (cyclohexyl ring carbons) δ 21.23 (methyl carbon).

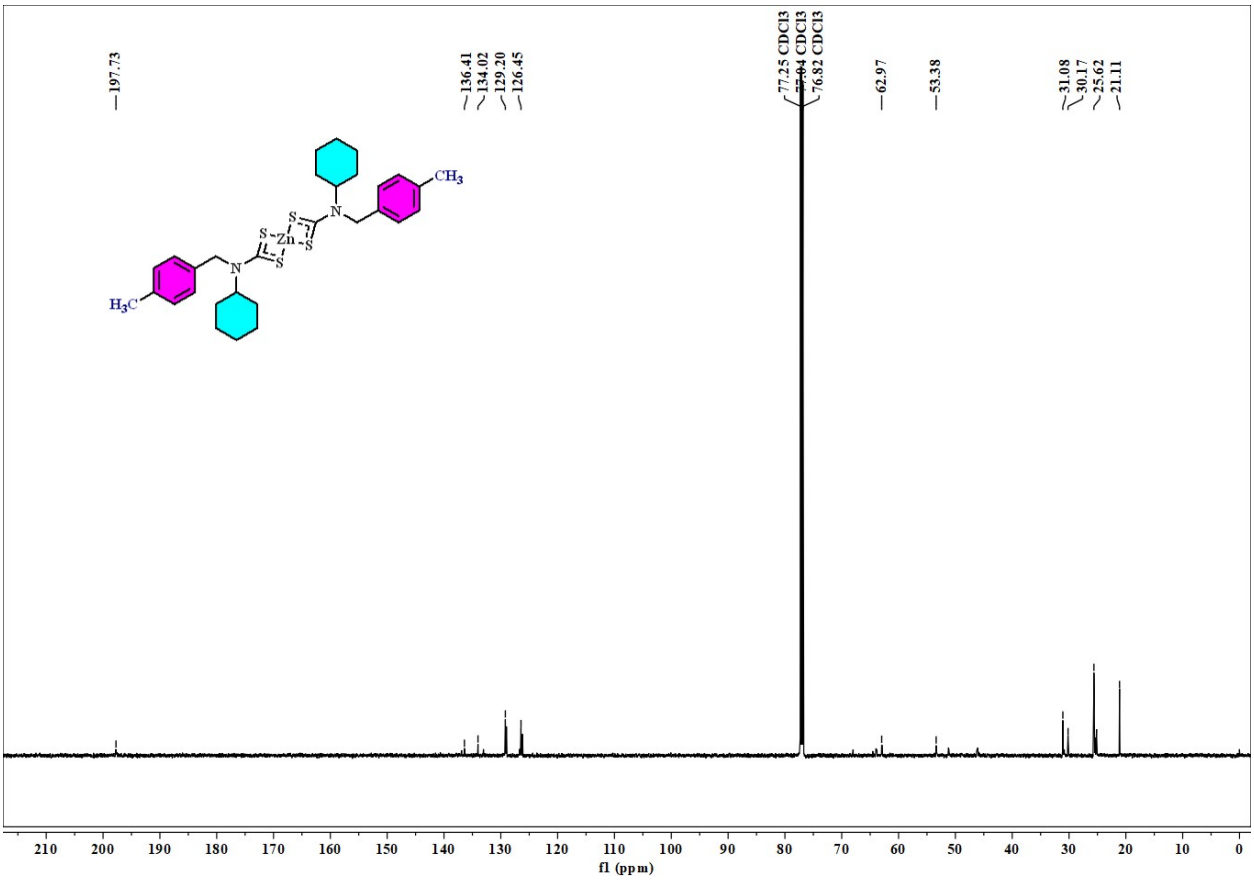

Figure S30. ^{13}C NMR spectrum of complex **3c**. $^{13}C\{^{1}H\}$ NMR (150 MHz, $CDCl_3$, ppm): δ 197.73 ($-CS_2$), δ 136.41, 134.02, 129.20, 126.45 (aromatic carbons), δ 53.38 (methylene), δ 62.97, 31.08, 30.17, 25.62 (cyclohexyl ring carbons) δ 21.11 (methyl carbon).

3. Magnetic and electronic spectral studies:

Magnetic susceptibility measurements at room temperature were performed using a Cahn-Faraday Electrobalance, calibrated with $Hg[Co(NCS)_4]$. Nickel complexes **1-3a** and zinc complexes **1-3c** were found diamagnetic while copper complexes **1-3b** are paramagnetic and μ_{eff} values were found between 1.76-1.79 BM. The UV-vis absorption spectra of the ligands **1-3** and complexes **1a-c, 2a-c, and 3a-c** were recorded in DMSO at room temperature at 10^{-5} molar concentration (*d-d* transition showed at 10^{-4} M concentration). The UV-vis spectra of ligand **1** and its complexes **1a–c** are presented in Figure S31, ligand **2** and its complexes **2a–c** in Figure S33, and ligand **3** and its complexes **3a–c** in Figure S35. The electronic spectra, illustrating *d-d* transitions of complexes **1a–b**, **2a–b**, and **3a–b**, are presented in Figures S32, S34, and S36, respectively. Absorption spectra of ligands **1-3** and their metal complexes **1a-c**, **2a-c**, and **3a-c** showed strong and higher energy bands in the range of 270-330 nm due to л→л*/ intra ligand charge transfer (ILCT) while a lower energy medium intensity bands in the range of 340-440 nm due to n→л*/ ILCT. The UV-vis spectra of complexes **1a-b**, **2a-b**, and **3a-b** showed some additional lower energy weak intensity broad bands in the range of 520-660 nm due to the *d-d* transitions of central metal ions.

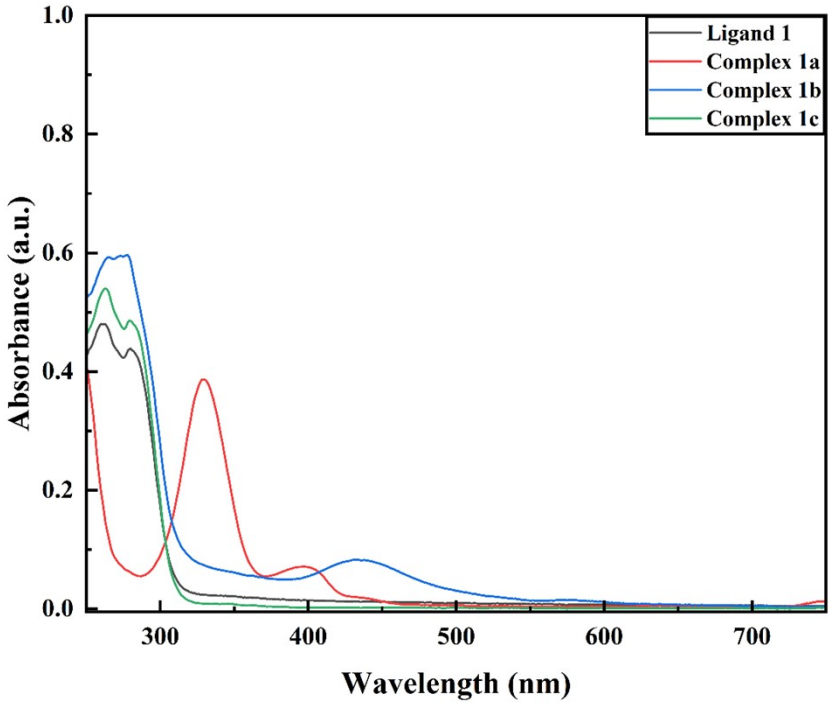

Figure S31. Absorption spectra of 10^{-5} M solution of ligand **1** and complexes **1a-c** in DMSO.

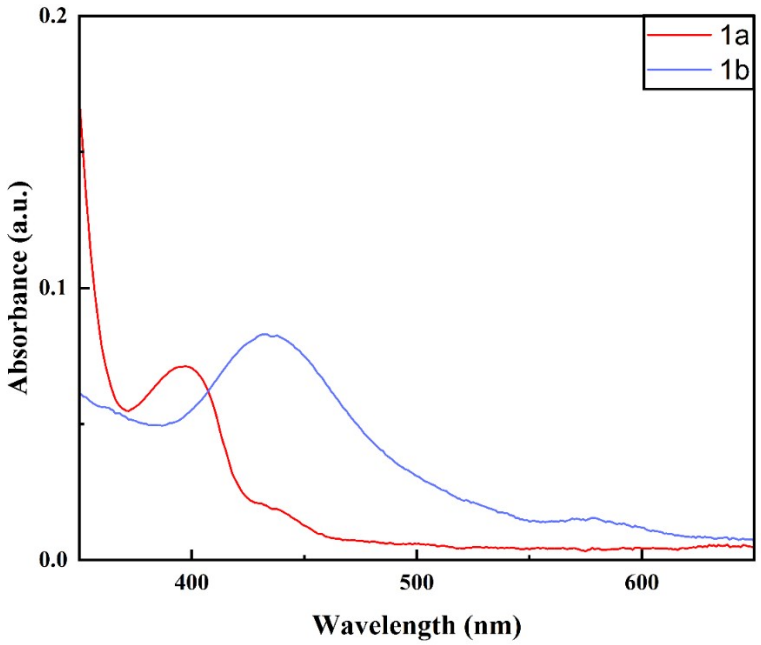

Figure S32. Absorption spectra showing *d-d* transition of complexes **1a** and **1b** in 10^{-4} M solution.

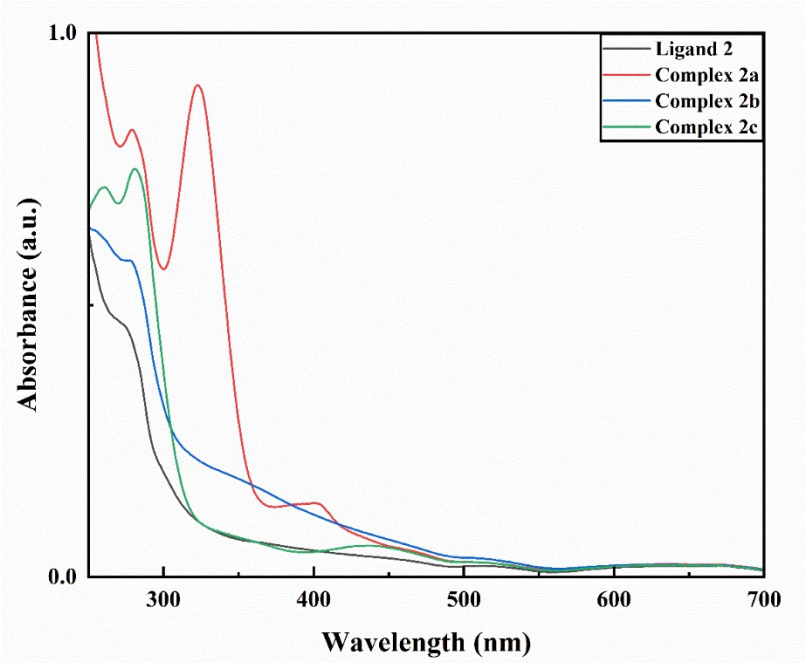

Figure S33. Absorption spectra of 10^{-5} M solution of ligand **2** and complexes **2a-c** in DMSO.

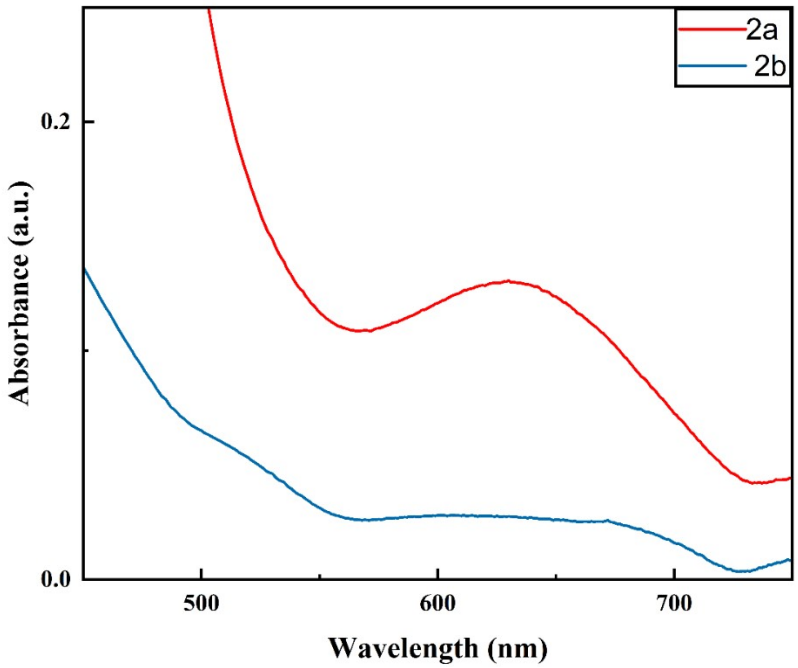

Figure S34. Absorption spectra showing d-d transition of complexes **2a** and **2b** in 10^{-4} M solution .

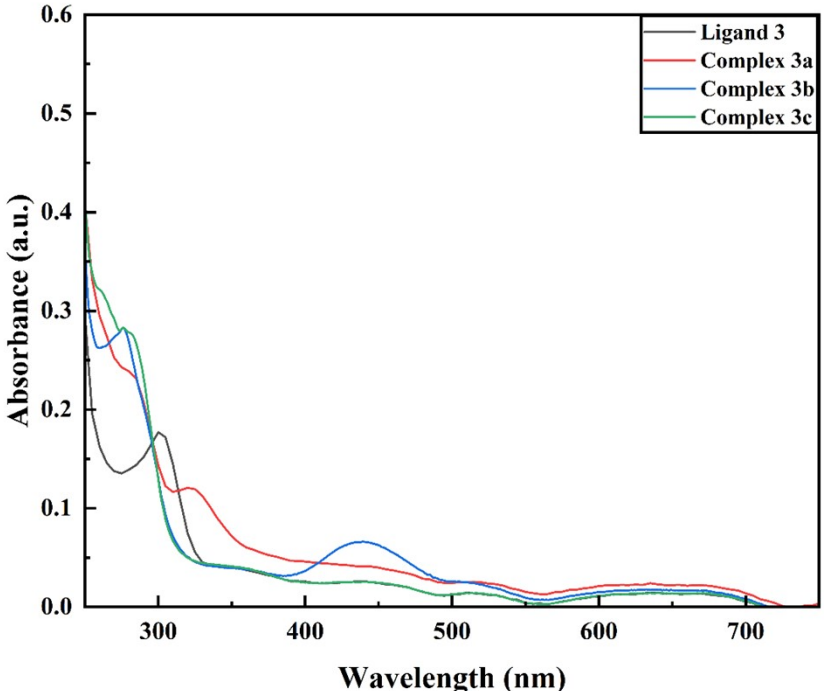

Figure S35. Absorption spectra of 10^{-5} M solution of ligand **3** and complexes **3a-c** in DMSO.

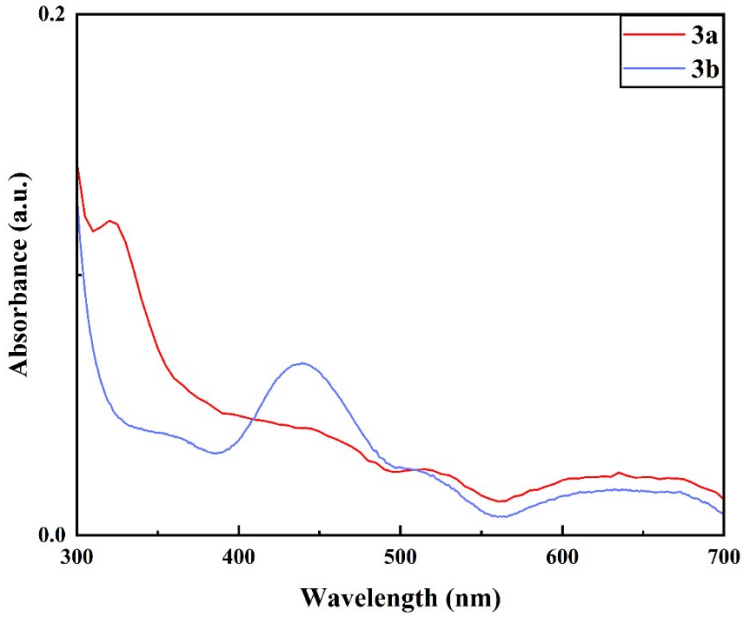

Figure S36. Absorption spectra showing *d-d* transition of complexes **3a** and **3b** in 10^{-4} M solution.

4. Mass spectra:

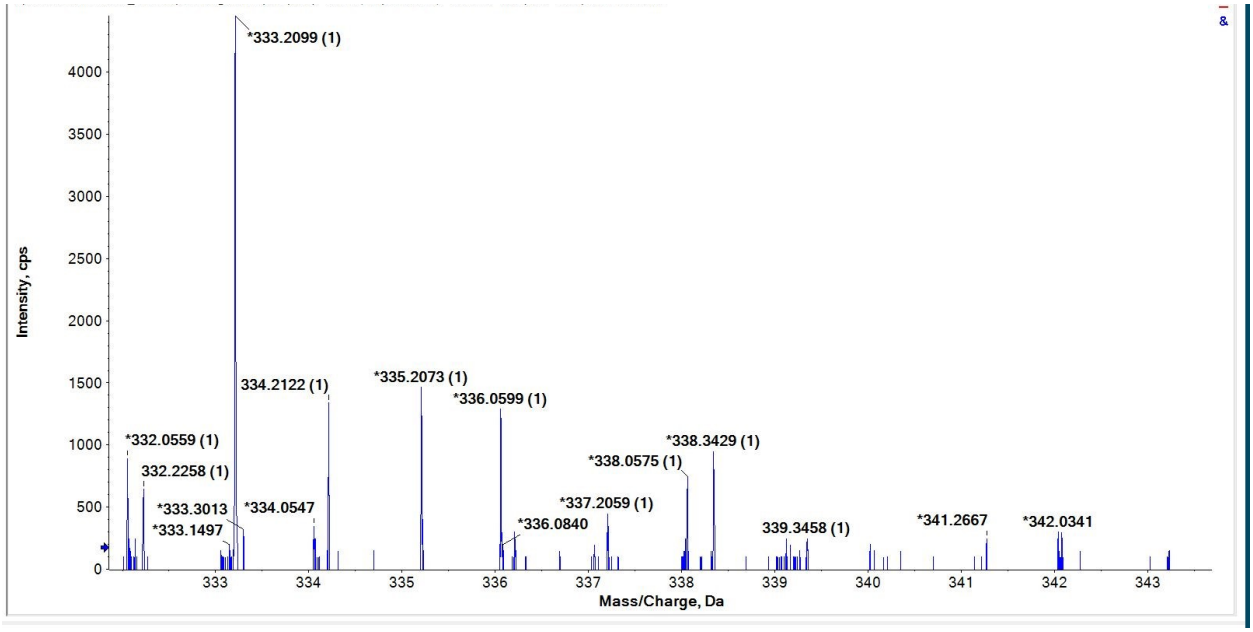

Figure S37. Mass spectrum of ligand **1**. calcd. m/z for $[M]^+$= 337.0128, found m/z for $[M]^+$= 337.2059, calcd. m/z for $[M+H]^+$= 338.0201, found m/z for $[M+H]^+$= 338.0575.

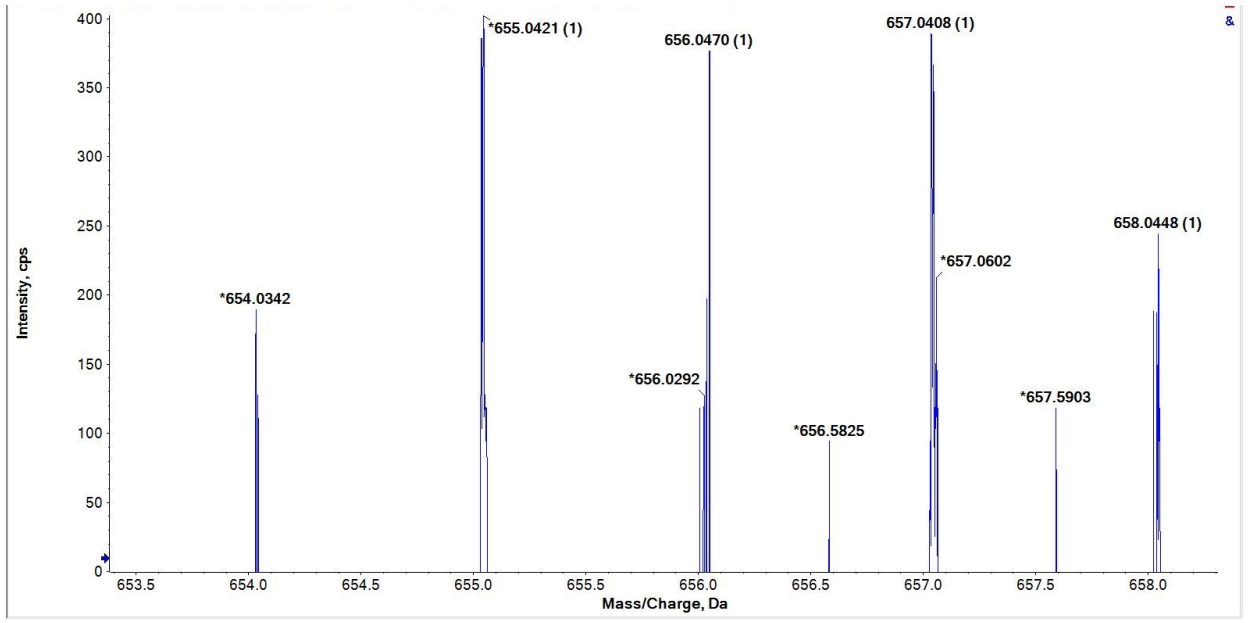

Figure S38. Mass spectrum of complex **1a**. calcd. m/z for $[M]^+$= 654.0335, found m/z for $[M]^+$= 654.0342, calcd. m/z for $[M+H]^+$= 655.0409, found m/z for $[M+H]^+$= 655.0421.

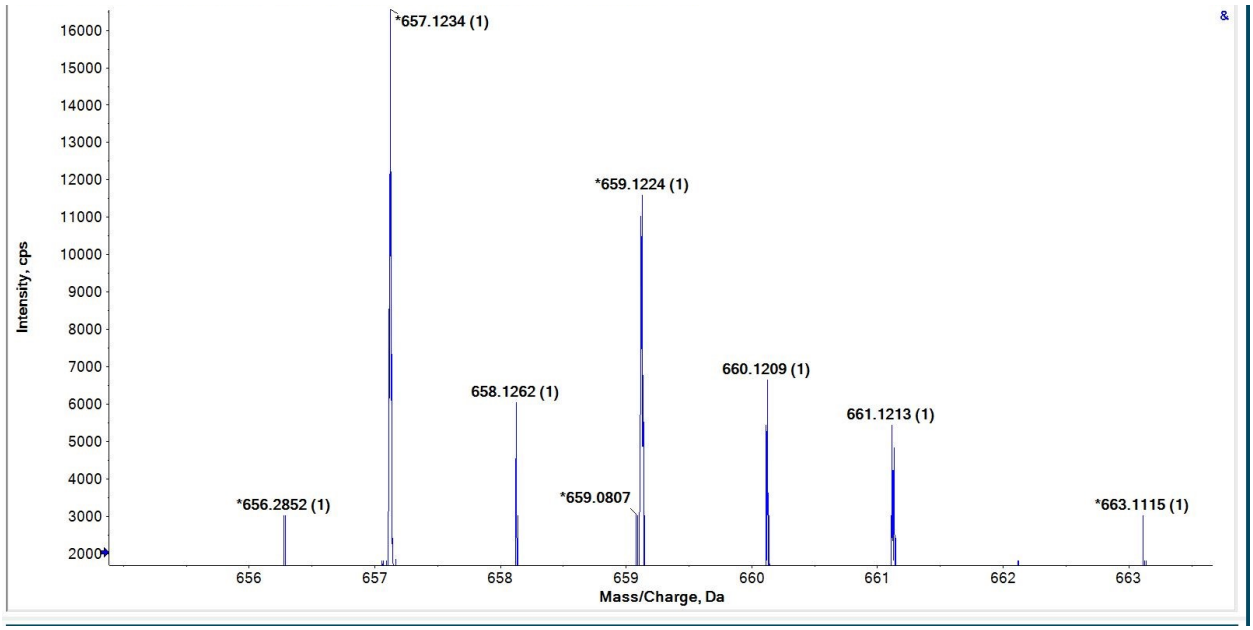

Figure S39. Mass spectrum of complex **1b**. calcd. m/z for $[M]^+$= 659.0278, found m/z for $[M]^+$= 659.1224, calcd. m/z for $[M+H]^+$= 660.0351, found m/z for $[M+H]^+$= 660.1209.

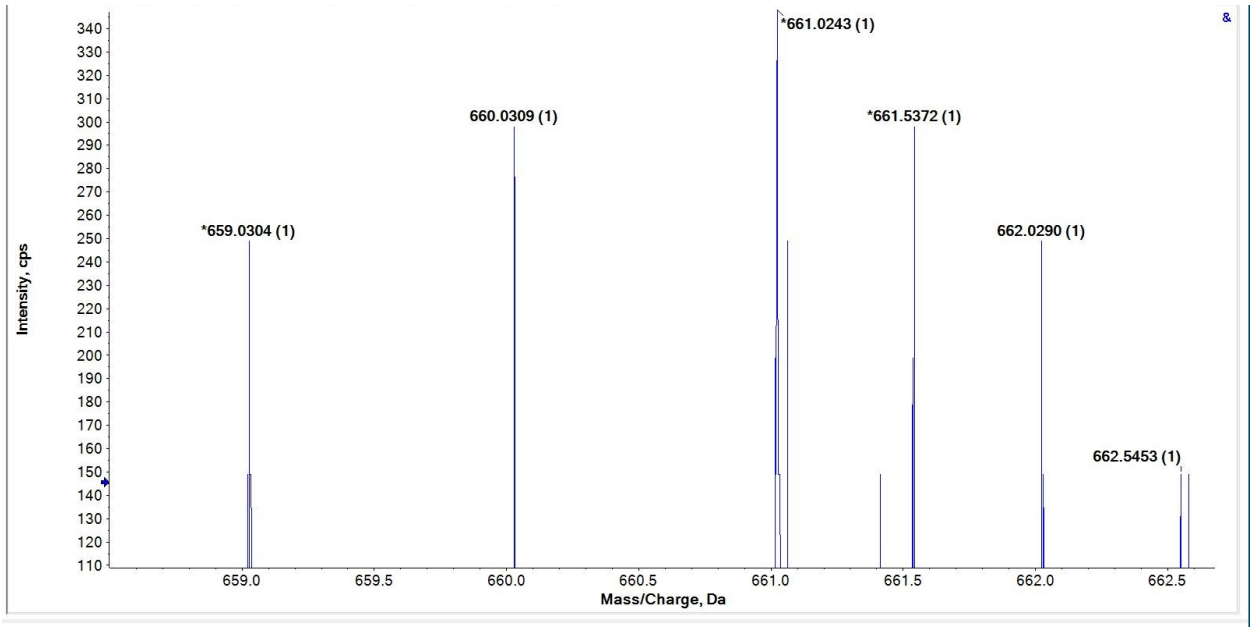

Figure S40. Mass spectrum of complex **1c**. calcd. m/z for $[M]^+$= 660.0273, found m/z for $[M]^+$= 660.0309, calcd. m/z for $[M+H]^+$= 661.0347, found m/z for $[M+H]^+$= 661.0243.

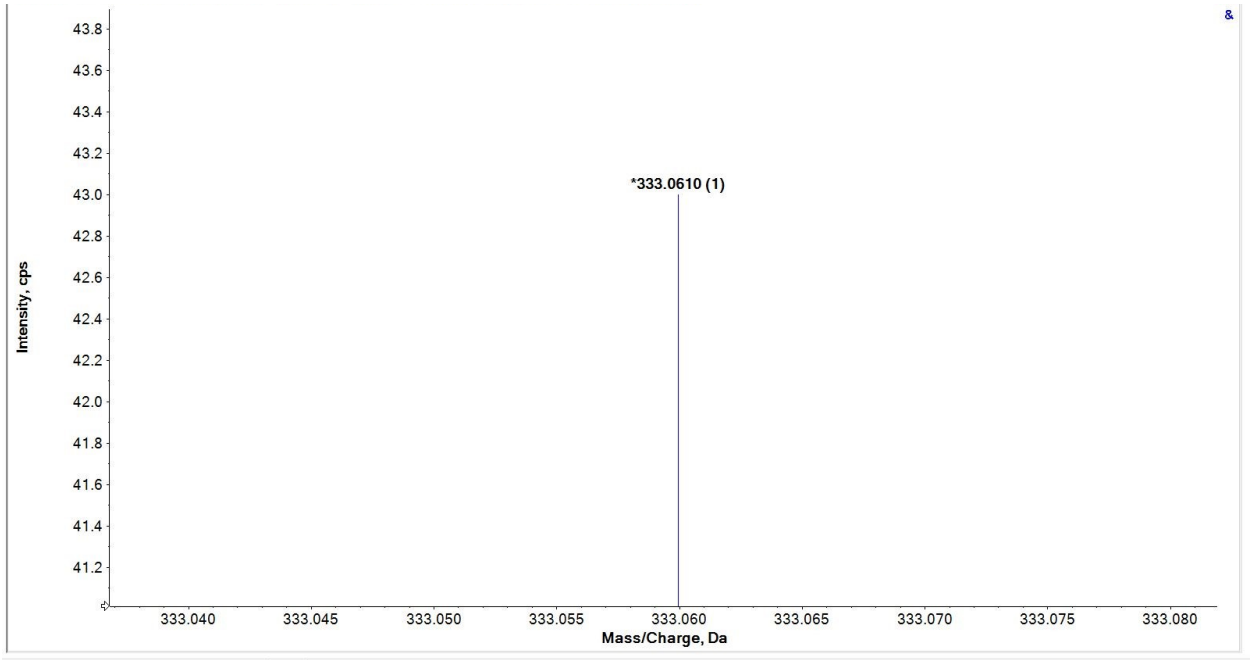

Figure S41. Mass spectrum of ligand **2**. calcd. m/z for $[M]^+$= 333.0623, found m/z for $[M]^+$= 333.0610.

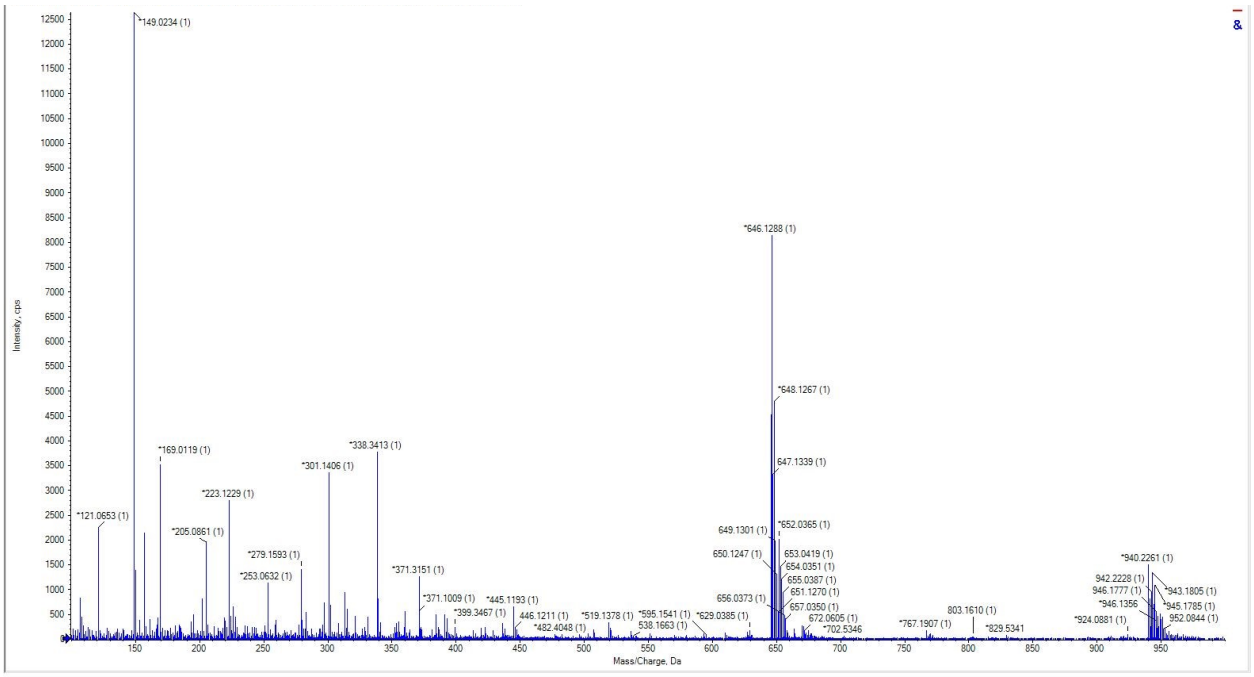

Figure S42. Mass spectrum of complex **2a**. calcd. m/z for $[M]^+$= 646.1326, found m/z for $[M]^+$= 646.1288.

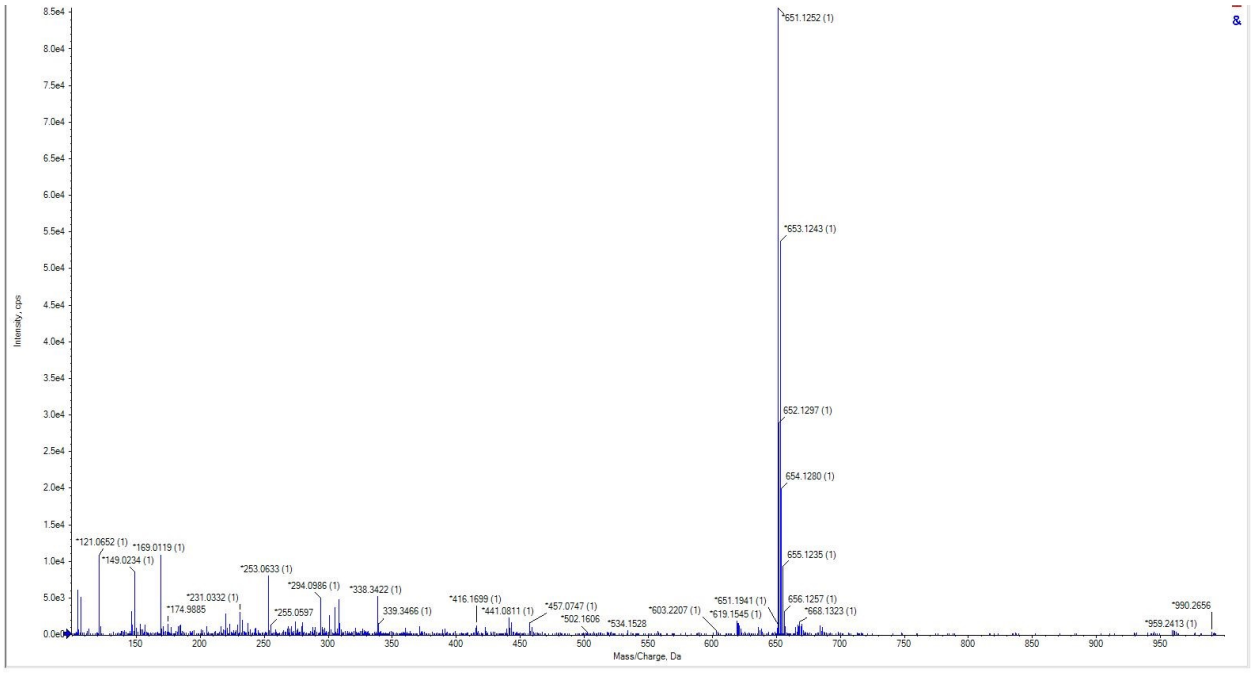

Figure S43. Mass spectrum of complex **2b**. calcd. m/z for $[M]^+$= 651.1269, found m/z for $[M]^+$= 651.1252.

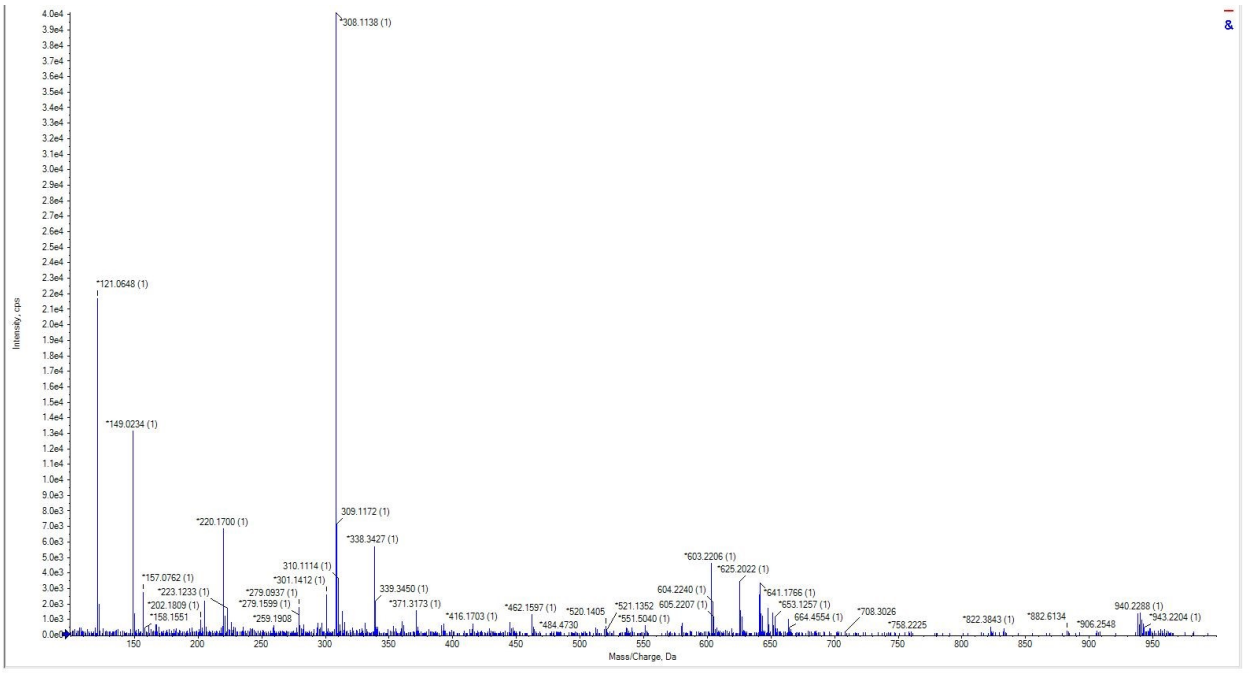

Figure S44. Mass spectrum of complex **2c**. calcd. m/z for $[M+H]^+$= 653.1337, found m/z for $[M+H]^+$= 653.1257.

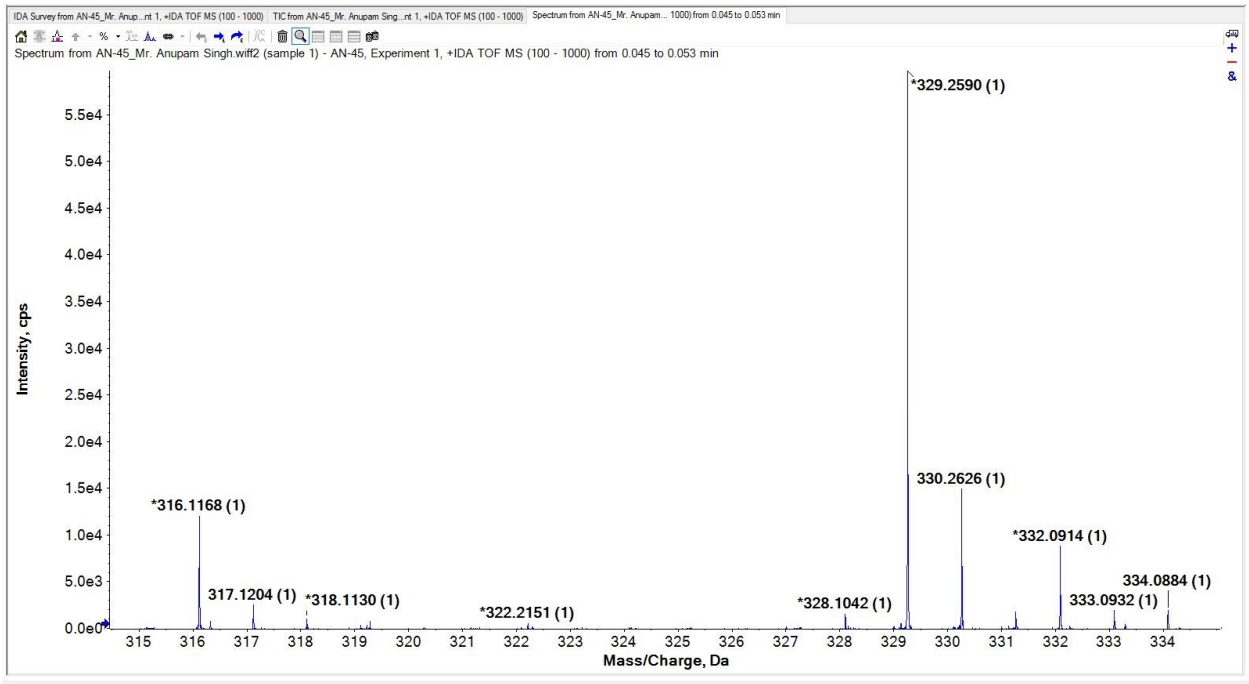

Figure S45. Mass spectrum of ligand **3**. calcd. m/z for $[M]^+$= 317.0674, found m/z for $[M]^+$= 317.1204, calcd. m/z for $[M+H]^+$= 318.0747, found m/z for $[M+H]^+$= 318.1130.

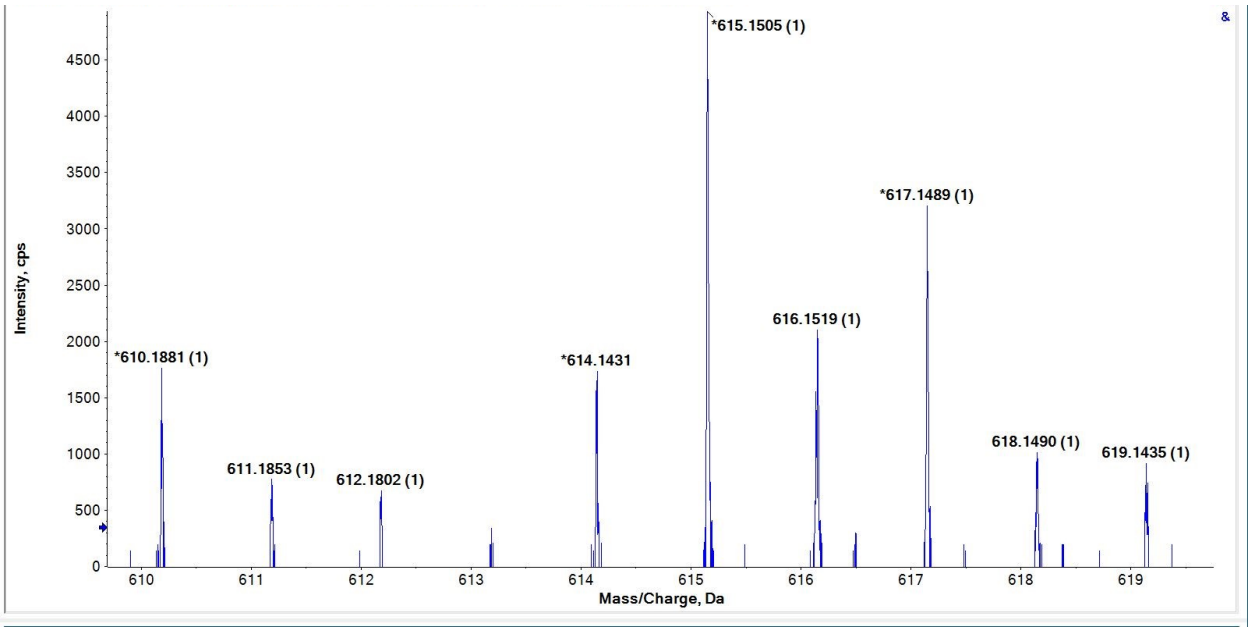

Figure S46. Mass spectrum of complex **3a**. calcd. m/z for $[M]^+$= 614.1428, found m/z for $[M]^+$= 614.1431, calcd. m/z for $[M+H]^+$= 615.1501, found m/z for $[M+H]^+$= 615.1505.

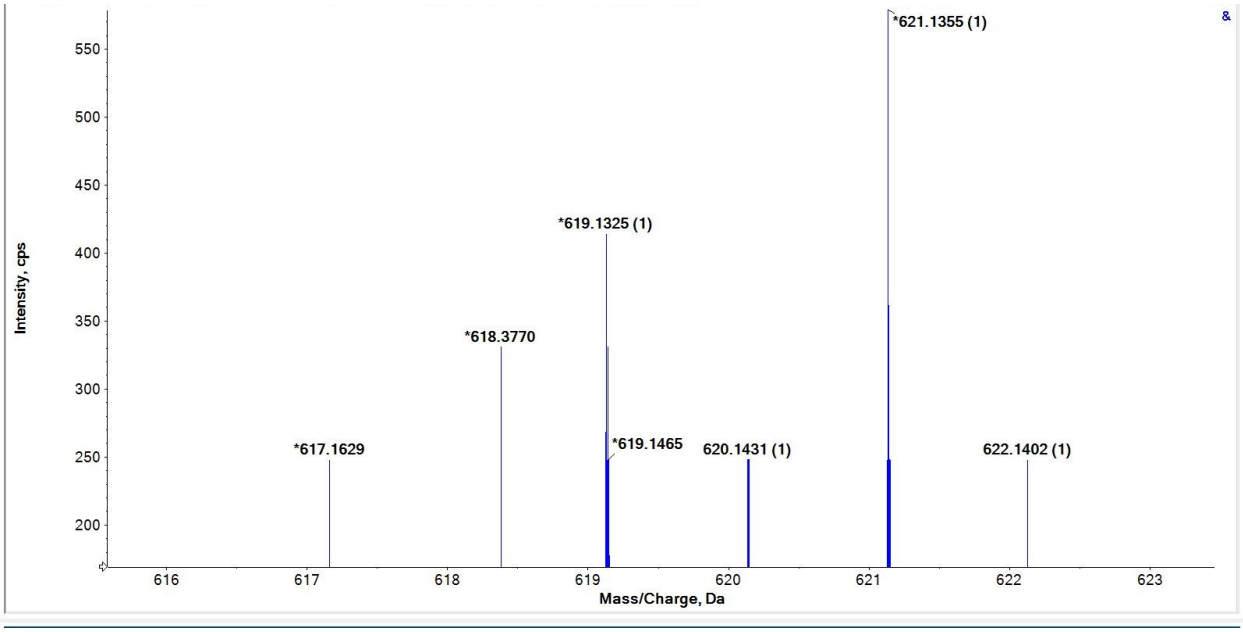

Figure S47. Mass spectrum of complex **3b**. calcd. m/z for $[M]^+$= 619.1370, found m/z for $[M]^+$= 619.1325, calcd. m/z for $[M+H]^+$= 620.1444, found m/z for $[M+H]^+$= 620.1431.

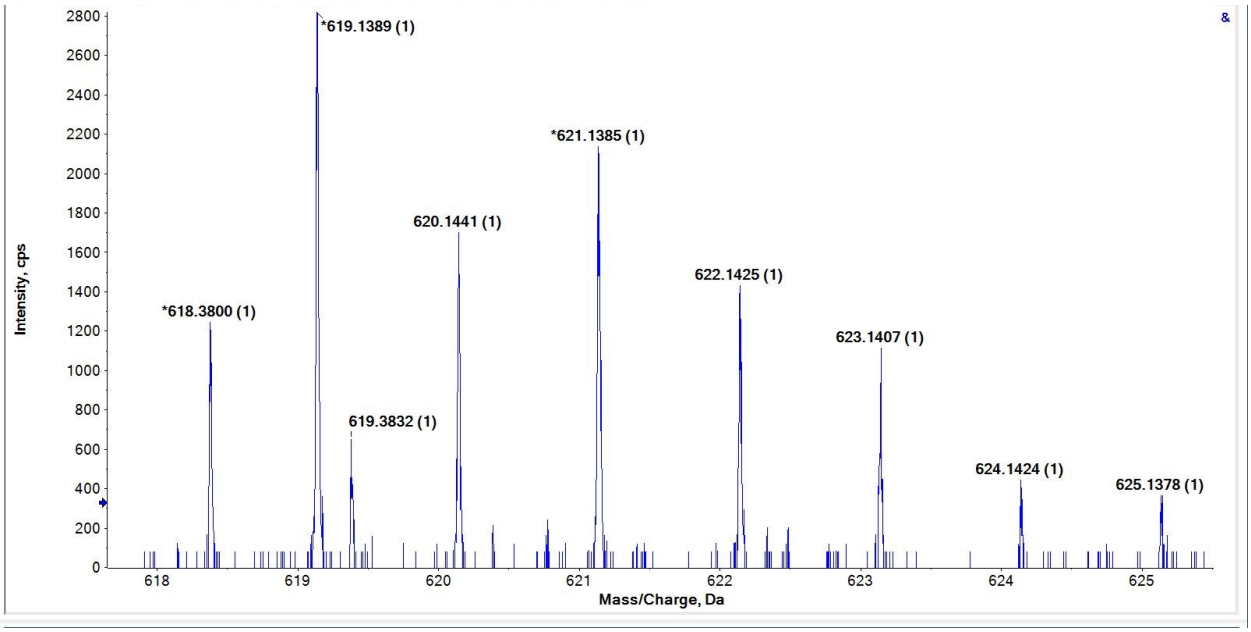

Figure S48. Mass spectrum of complex **3c**. calcd. m/z for $[M]^+$= 620.1366, found m/z for $[M]^+$= 620.1441, calcd. m/z for $[M+H]^+$= 621.1439, found m/z for $[M+H]^+$= 621.1385.

5. Stability and Thermogravimetric Analysis

In our preliminary experiment, we have checked the stability of the compound in simulated body fluid (SBF) and found that the compound remain stable and not affected by the physiologically similar fluid to that of plasma or any other body fluid, the compound may encounter during its *in vivo* treatment situation. We have also observed that slightly or no acidic environment of the plate bound tumor cell based assay did not alter the condition or stability of the metal coordinate complexes. In *in vivo* tumor proximity state, the materials were also unaffected and remain stable indicating that the compound remain intact in tumoricidal potential reported by us. We have also thermal stability by thermogravimetric analysis. Overall, its is observed that the compound remain unaffected by the physiological condition like low pH, supposed to occur in tumor vicinity when the compounds were given for antitumor activity.

Thermogravimetric Analysis (TGA)

The thermal behavior of metal complexes **1a–c**, **2a–c**, and **3a–c** was systematically investigated using thermogravimetric analysis (TGA) under an inert nitrogen atmosphere. The TGA experiments were conducted over a temperature range of 30–700 °C at a constant heating rate of 10 °C min^{-1}. The corresponding TGA curves are illustrated in **Figures**. S49-51. All the complexes

exhibited a comparable two-step thermal decomposition profile, indicating a consistent decomposition pattern across the series. The initial mass loss, occurring below 100 °C, ranged between 3–5% and can be attributed to the desorption of physically adsorbed moisture or the loss of loosely bound solvent molecules.

The first significant decomposition event was observed between 150 °C and 300 °C, characterized by a sharp weight loss of approximately 65–70%. This substantial weight reduction is indicative of the decomposition of the organic backbone of the dithiocarbamate ligands. The breakdown of C–N, C–S, and other organic functionalities leads to the release of volatile organic fragments, signifying the thermal instability of the ligand framework in this temperature range. The second decomposition stage was noted beyond 300 °C, involving a slower and more gradual weight loss of about 8–10%. This phase likely corresponds to the elimination of residual organic fragments or secondary degradation products from the initial decomposition, including carbonaceous residues or partially oxidized species. After 500 °C, the TGA traces for all the complexes showed a plateau region with negligible further mass loss, suggesting the completion of thermal degradation. The residual mass at this stage, approximately 12–15% of the original sample weight, is attributed to the formation of thermally stable metal sulfide species. These residues are consistent with the expected metal sulfide products resulting from the decomposition of metal–sulfur bonds in the dithiocarbamate framework.

The final residues and thermal decomposition profile align well with literature-reported data on dithiocarbamate-based complexes, reinforcing the hypothesis that these compounds can serve as single-source precursors for the generation of metal sulfide nanoparticles. The controlled decomposition and defined thermal events observed further support the potential utility of these complexes in applications requiring thermally induced metal sulfide formation, such as in materials science and nanotechnology.

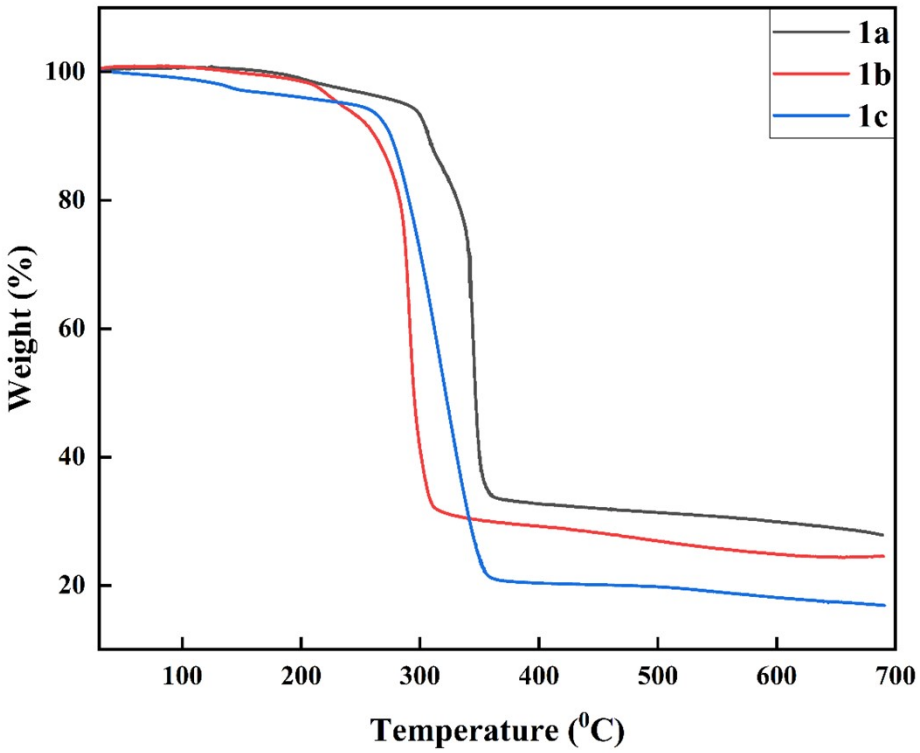

Figure S49. TGA plot of complexes **1a-c**.

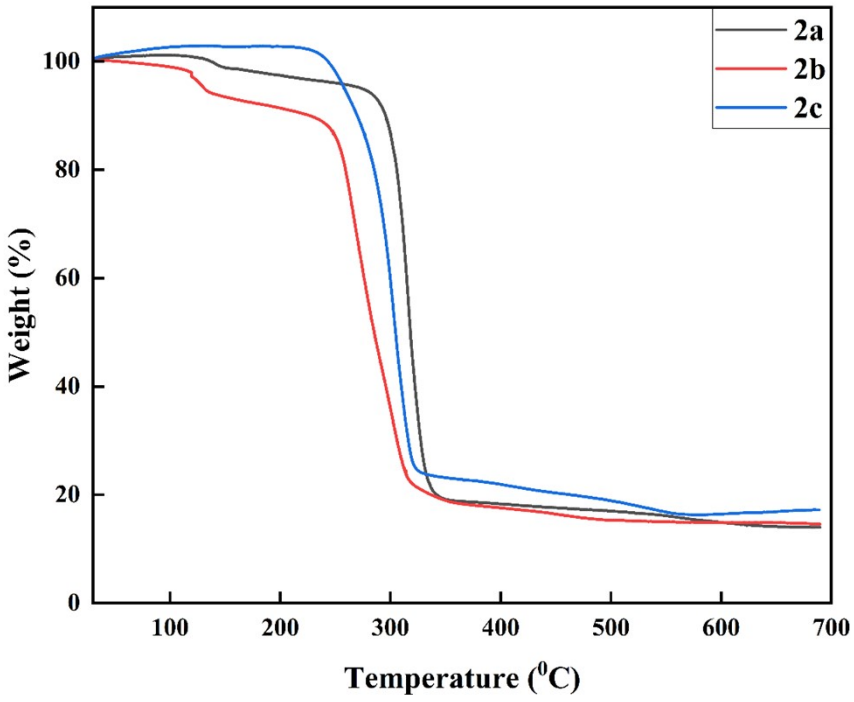

Figure S50. TGA plot of complexes **2a-c**.

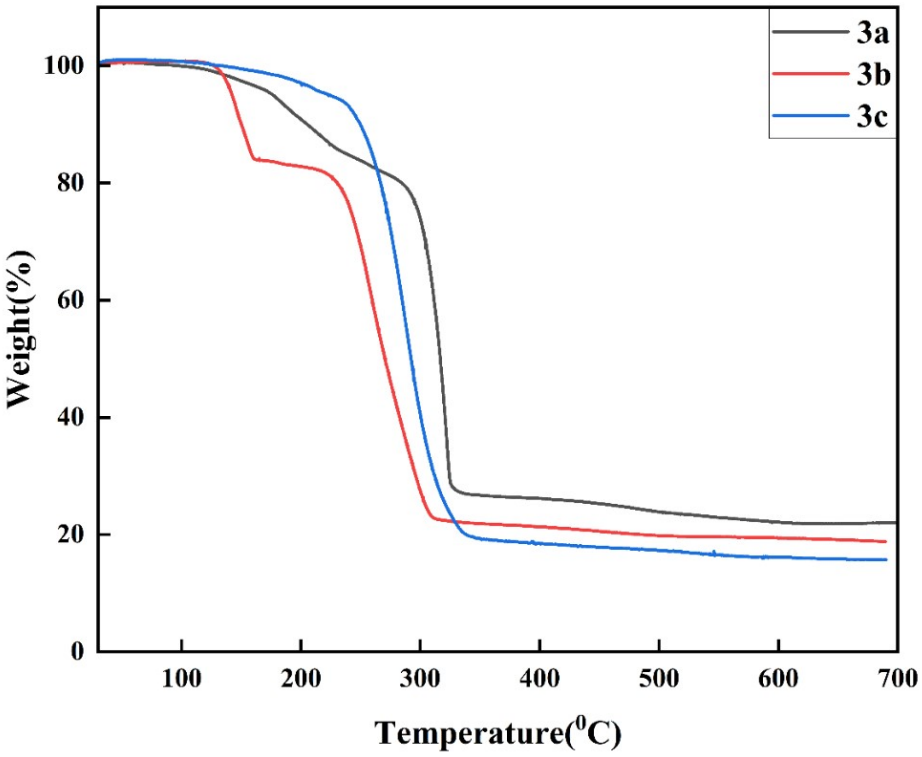

Figure S51. TGA plot of complexes **3a-c**.

6. X-ray crystallography:

X-ray diffraction measurements of complexes **1a-b, 2b-c,** and **3a-c** were performed using Oxford Gemini and Bruker three-circle diffractometer equipped with a CrysAlisPro/CrysAlis CCD software using a graphite mono-chromated Mo/Cu Kα (λ= 0.71073/1.54184 Å) radiation source at 296 K. The details of the temperature and monochromator of diffractometers are mentioned in the crystallographic data tables. Multi-scan absorption correction was applied to the X-ray data collection for all the compounds. The structures were solved by direct methods (SHELXS-08) and refined against all data by full matrix least-square on F^2 using anisotropic displacement parameters for all non-hydrogen atoms. All hydrogen atoms were included in the refinement at geometrically ideal positions and refined with a riding model[1]. The MERCURY package and ORTEP-3 for Windows program were used for generating structures[2,3].

Table S1. Bond length (Å) and angles (°) for complex **1a**

Bond length (Å)		**Bond angle (º)**	
Ni-S(2)#1	2.2020(7)	S(2)#1-Ni-S(1)	100.82(3)
Ni-S(2)	2.2020(7)	S(2)-Ni-S(1)	79.18(3)
Ni-S(1)	2.2044(8)	S(2)#1-Ni-S(1)#1	79.18(3)
Ni-S(1)#1	2.2044(8)	S(2)-Ni-S(1)#1	100.82(3)
S(2)-C(1)	1.724(3)	C(1)-S(2)-Ni	85.52(9)
S(1)-C(1)	1.713(3)	C(1)-S(1)-Ni	85.71(10)
Cl(1)-C(6)	1.741(3)	C(1)-N(1)-C(2)	119.0(2)
N(1)-C(1)	1.319(3)	C(1)-N(1)-C(9)	120.9(2)
N(1)-C(2)	1.473(3)	C(2)-N(1)-C(9)	119.1(2)
N(1)-C(9)	1.489(3)	N(1)-C(1)-S(1)	125.1(2)

Symmetry transformations used to generate equivalent atoms: #1 -x,-y+1,-z+1

Table S2. Bond length (Å) and angles (°) for complex **1b**

Bond length (Å)		**Bond angle (º)**	
Cu-S(2)#1	2.3034(7)	S(2)#1-Cu-S(1)	102.84(3)
Cu-S(2)	2.3034(7)	S(2)-Cu-S(1)	77.16(3)
Cu-S(1)	2.3038(9)	S(2)#1-Cu-S(1)#1	77.16(3)
Cu-S(1)#1	2.3038(9)	S(2)-Cu-S(1)#1	102.84(3)
S(1)-C(1)	1.727(3)	S(1)-Cu-S(1)#1	180.0
S(2)-C(1)	1.725(3)	C(1)-S(1)-Cu	85.01(11)
Cl(1)-C(6)	1.740(3)	C(1)-S(2)-Cu	85.07(10)
N(1)-C(1)	1.306(4)	C(1)-N(1)-C(2)	120.0(2)
N(1)-C(2)	1.482(4)	C(1)-N(1)-C(9)	121.5(2)
N(1)-C(9)	1.495(3)	C(2)-N(1)-C(9)	117.8(3)

Symmetry transformations used to generate equivalent atoms: #1 -x,-y+1,-z+1

Table S3. Bond length (Å) and angles (°) for complex **2b**

Bond length (Å)		**Bond angle (º)**	
Cu(1)-S(4A)	2.285(4)	S(4A)-Cu(1)-S(2A)	102.06(13)
Cu(1)-S(2A)	2.289(3)	S(4A)-Cu(1)-S(3A)	77.88(12)
Cu(1)-S(3A)	2.292(3)	S(2A)-Cu(1)-S(3A)	178.07(18)
Cu(1)-S(1A)	2.300(4)	S(4A)-Cu(1)-S(1A)	174.65(16)
S(1A)-C(1A)	1.703(13)	S(2A)-Cu(1)-S(1A)	77.03(13)
S(2A)-C(1A)	1.700(12)	S(3A)-Cu(1)-S(1A)	103.21(13)
S(3A)-C(16A)	1.740(11)	C(1A)-S(1A)-Cu(1)	84.1(4)
S(4A)-C(16A)	1.702(11)	C(1A)-S(2A)-Cu(1)	84.5(5)
O(1A)-C(6A)	1.33(2)	C(16A)-S(3A)-Cu(1)	83.7(4)
O(1A)-C(9A)	1.46(3)	C(16A)-S(4A)-Cu(1)	84.7(4)
O(2A)-C(21A)	1.36(2)	S(4A)-Cu(1)-S(2A)	102.06(13)
O(2A)-C(24A)	1.49(2)	S(4A)-Cu(1)-S(3A)	77.88(12)
N(1A)-C(1A)	1.357(17)	S(2A)-Cu(1)-S(3A)	178.07(18)
N(1A)-C(10A)	1.446(19)	S(4A)-Cu(1)-S(1A)	174.65(16)
N(1A)-C(2A)	1.511(15)	N(1A)-C(1A)-S(2A)	124.6(9)
N(2A)-C(16A)	1.372(15)	N(1A)-C(1A)-S(1A)	121.0(9)
N(2A)-C(25A)	1.446(15)	S(2A)-C(1A)-S(1A)	114.3(7)
N(2A)-C(17A)	1.471(17)	C(3A)-C(2A)-N(1A)	112.7(11)

Table S4. Bond length (Å) and angles (°) for complex **2c**

Bond length (Å)		**Bond angle (º)**	
Zn(1)-S(1A)	2.3438(4)	S(1A)-Zn(1)-S(3A)	132.759(18)
Zn(1)-S(3A)	2.3465(4)	S(1A)-Zn(1)-S(2A)#1	105.877(15)
Zn(1)-S(2A)#1	2.3819(4)	S(3A)-Zn(1)-S(2A)#1	119.564(16)
Zn(1)-S(4A)	2.4694(4)	S(1A)-Zn(1)-S(4A)	101.053(15)
Zn(1)-S(2A)	2.7761(4)	S(3A)-Zn(1)-S(4A)	75.281(14)
S(1A)-C(1A)	1.7224(14)	S(2A)#1-Zn(1)-S(4A)	111.019(16)
S(2A)-C(1A)	1.7498(14)	S(1A)-Zn(1)-S(2A)	69.744(12)
S(3A)-C(16A)	1.7340(15)	S(3A)-Zn(1)-S(2A)	98.099(14)
S(4A)-C(16A)	1.7181(15)	S(2A)#1-Zn(1)-S(2A)	88.179(13)
O(1A)-C(6A)	1.374(2)	S(4A)-Zn(1)-S(2A)	160.605(15)
O(1A)-C(9A)	1.420(2)	C(1A)-S(1A)-Zn(1)	93.64(5)
O(2A)-C(21A)	1.370(2)	C(1A)-S(2A)-Zn(1)#1	101.66(4)
O(2A)-C(24A)	1.420(3)	C(1A)-S(2A)-Zn(1)	79.35(5)
N(1A)-C(1A)	1.3236(18)	Zn(1)#1-S(2A)-Zn(1)	91.822(13)
N(1A)-C(2A)	1.4835(18)	C(16A)-S(3A)-Zn(1)	85.48(5)
N(1A)-C(10A)	1.4933(17)	C(16A)-S(4A)-Zn(1)	82.02(5)
N(2A)-C(16A)	1.3339(18)	C(6A)-O(1A)-C(9A)	117.67(17)
N(2A)-C(17A)	1.469(2)	C(21A)-O(2A)-C(24A)	117.07(16)
N(2A)-C(25A)	1.488(2)	N(1A)-C(1A)-S(1A)	122.19(11)

Symmetry transformations used to generate equivalent atoms: #1 -x+2,-y,-z+1 #2 -x+1,-y+1,-z

Table S5. Bond length (Å) and angles (°) for complex **3a**

Bond length (Å)		**Bond angle (º)**	
Ni(1)-S(2)#1	2.1966(5)	S(2)#1-Ni(1)-S(1)#1	79.506(19)
Ni(1)-S(2)	2.1967(5)	S(2)-Ni(1)-S(1)#1	100.495(19)
Ni(1)-S(1)#1	2.1987(5)	S(2)#1-Ni(1)-S(1)	100.494(19)
Ni(1)-S(1)	2.1987(5)	S(2)-Ni(1)-S(1)	79.504(19)
Ni(2)-S(4)	2.1998(6)	S(4)-Ni(2)-S(3)#2	100.665(19)
Ni(2)-S(4)#2	2.1998(6)	S(4)#2-Ni(2)-S(3)#2	79.335(19)
Ni(2)-S(3)#2	2.2029(5)	S(4)-Ni(2)-S(3)	79.336(19)
Ni(2)-S(3)	2.2029(5)	S(4)#2-Ni(2)-S(3)	100.664(19)
S(3)-C(16)	1.719(2)	C(16)-S(3)-Ni(2)	85.49(7)
S(2)-C(1)	1.716(2)	C(1)-S(2)-Ni(1)	85.41(7)
S(1)-C(1)	1.719(2)	C(1)-S(1)-Ni(1)	85.28(7)
S(4)-C(16)	1.721(2)	C(16)-S(4)-Ni(2)	85.53(7)
N(1)-C(1)	1.322(3)	C(16)-N(2)-C(17)	119.81(17)
N(1)-C(2)	1.473(3)	C(16)-N(2)-C(25)	120.51(17)
N(1)-C(10)	1.483(3)	C(17)-N(2)-C(25)	119.21(17)
N(2)-C(16)	1.321(3)	N(2)-C(16)-S(3)	126.04(16)
N(2)-C(17)	1.471(3)	N(2)-C(16)-S(4)	124.39(16)
N(2)-C(25)	1.482(3)	S(3)-C(16)-S(4)	109.57(12)

Symmetry transformations used to generate equivalent atoms: #1 -x+2,-y+1,-z #2 -x+1,-y,-z+1

Table S6. Bond length (Å) and angles (°) for complex **3b**

Bond length (Å)		**Bond angle (º)**	
Cu(1)-S(1)#1	2.2673(7)	S(1)#1-Cu(1)-S(2)#1	77.42(2)
Cu(1)-S(1)	2.2673(7)	S(1)-Cu(1)-S(2)#1	102.58(2)
Cu(1)-S(2)#1	2.3295(7)	S(1)#1-Cu(1)-S(2)	102.58(2)
Cu(1)-S(2)	2.3295(7)	S(1)-Cu(1)-S(2)	77.42(2)
S(1)-C(1)	1.728(3)	C(1)-S(1)-Cu(1)	85.61(9)
S(2)-C(1)	1.724(3)	C(1)-S(2)-Cu(1)	83.77(9)
N(1)-C(1)	1.318(3)	C(1)-N(1)-C(10)	120.0(2)
N(1)-C(2)	1.483(3)	N(1)-C(1)-S(2)	124.3(2)
N(1)-C(10)	1.486(3)	S(2)-C(1)-S(1)	112.77(16)

Symmetry transformations used to generate equivalent atoms: #1 -x+2,-y,-z

Table S7. Bond length (Å) and angles (°) for complex **3c**

Bond length (Å)		**Bond angle (º)**	
Zn(1)-S(2B)	2.3288(12)	S(2B)-Zn(1)-S(1A)	128.70(5)
Zn(1)-S(1A)	2.3291(11)	S(2B)-Zn(1)-S(1B)	78.22(4)
Zn(1)-S(1B)	2.3369(12)	S(1A)-Zn(1)-S(1B)	130.01(5)
Zn(1)-S(2A)	2.3611(13)	S(2B)-Zn(1)-S(2A)	125.71(5)
S(1A)-C(1A)	1.722(5)	S(1A)-Zn(1)-S(2A)	78.14(4)
S(2A)-C(1A)	1.741(4)	S(1B)-Zn(1)-S(2A)	123.53(5)
N(1A)-C(1A)	1.330(5)	C(1A)-S(1A)-Zn(1)	82.95(14)
N(1A)-C(10C)	1.415(18)	C(1A)-S(2A)-Zn(1)	81.61(15)
N(1A)-C(2A)	1.425(16)	C(1A)-N(1A)-C(10C)	125.9(8)
N(1A)-C(10A)	1.536(12)	N(1A)-C(1A)-S(1A)	121.5(3)
N(1A)-C(2C)	1.537(13)	S(1A)-C(1A)-S(2A)	117.2(2)

Table S8. Hydrogen bond parameters for Complex **1a and 1b**.

D-H···A	d(D-H)	d(H···A)	d(D···A)	<(DHA)
C(9)-H(9)···S(2)	0.98	2.51	3.087(3)	117.4
Complex-**1b**				
C(9)-H(9)···S(2)	0.98	2.49	3.061(3)	117.0

Symmetry transformations used to generate equivalent atoms:

#1 -x,-y+1,-z+1

Table S9. Hydrogen bond parameters for Complex **2b**.

D-H···A	d(D-H)	d(H···A)	d(D···A)	<(DHA)
C(2A)-H(2AB)···S(2A)	0.97	2.56	3.081(15)	113.7
C(2B)-H(2BA)···S(2B)	0.97	2.50	2.992(14)	111.2
C(15B)-H(15C)···S(1B)	0.97	3.01	3.537(16)	115.4
C(17B)-H(17D)···S(4B)	0.97	2.45	3.023(17)	117.4
C(30B)-H(30C)···S(3B)	0.97	3.01	3.527(17)	114.5

Table S10. Hydrogen bond parameters for Complex **2c**.

D-H···A	d(D-H)	d(H···A)	d(D···A)	<(DHA)
C(2A)-H(2AB)···S(1A)	0.97	2.55	3.0188(15)	110.0
C(10A)-H(10A)···S(2A)	0.98	2.50	3.0213(15)	113.0
C(25A)-H(25A)···S(3A)	0.98	2.47	3.0355(15)	116.1
C(9B)-H(9BC)···S(3A)#3	0.96	3.00	3.939(3)	167.2
C(10B^a)-H(10B^a)···S(2B)	0.98	2.49	2.997(6)	111.7
C(10D^b)-H(10C^b)···S(2B)	0.98	2.35	2.972(17)	120.8
C(17B)-H(17D)···S(3B)	0.97	2.52	3.0342(15)	112.7
C(25B)-H(25B)···S(4B)	0.98	2.47	2.9727(15)	111.2

Symmetry transformations used to generate equivalent atoms:

#1 -x+2,-y,-z+1 #2 -x+1,-y+1,-z #3 -x+2,y+1/2,-z+1/2

Table S11. Hydrogen bond parameters for Complex **3a**.

D-H···A	d(D-H)	d(H···A)	d(D···A)	<(DHA)
C(25)-H(25)···S(3)	0.98	2.58	3.089(2)	112.7
C(10)-H(10)···S(2)	0.98	2.54	3.079(2)	114.4

Symmetry transformations used to generate equivalent atoms:

#1 -x+2,-y+1,-z #2 -x+1,-y,-z+1

Table S12. Hydrogen bond parameters for Complex **3b**.

D-H···A	d(D-H)	d(H···A)	d(D···A)	<(DHA)
C(2)-H(2A)···S(1)	0.99	2.49	3.018(3)	112.7
C(15)-H(15A)···N(1)#2	0.99	2.70	3.672(4)	168.3
C(11)-H(11A)···S(2)	0.99	3.03	3.535(3)	113.2

Symmetry transformations used to generate equivalent atoms:

#1 -x+2,-y,-z #2 -x+1,-y+1,-z

Table S13. Hydrogen bond parameters for Complex **3c**.

D-H···A	d(D-H)	d(H···A)	d(D···A)	<(DHA)
C(2C^b)-H(2CA^b)···S(1A)	0.97	2.33	2.873(11)	114.8
C(2C^b)-H(2CA^b)···S(2B)#1	0.97	2.98	3.727(13)	134.5
C(11C^b)-H(11D^b)···S(2A)	0.97	2.99	3.523(12)	116.0
C(2B)-H(2BA)···S(1B)#2	1.04(4)	2.88(4)	3.844(4)	154(3)

Symmetry transformations used to generate equivalent atoms:

#1 x,-y+1/2,z-1/2 #2 x,-y+3/2,z+1/2

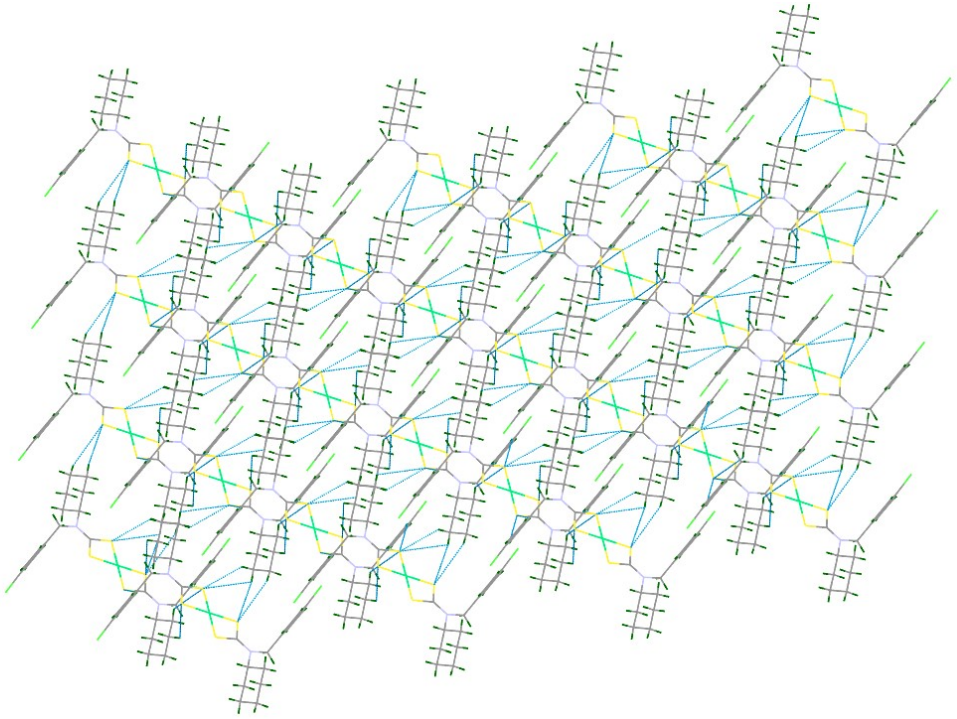

Figure S52. Showing C-H···S hydrogen bonding interactions leading to a ladder-like architecture complex **1a**.

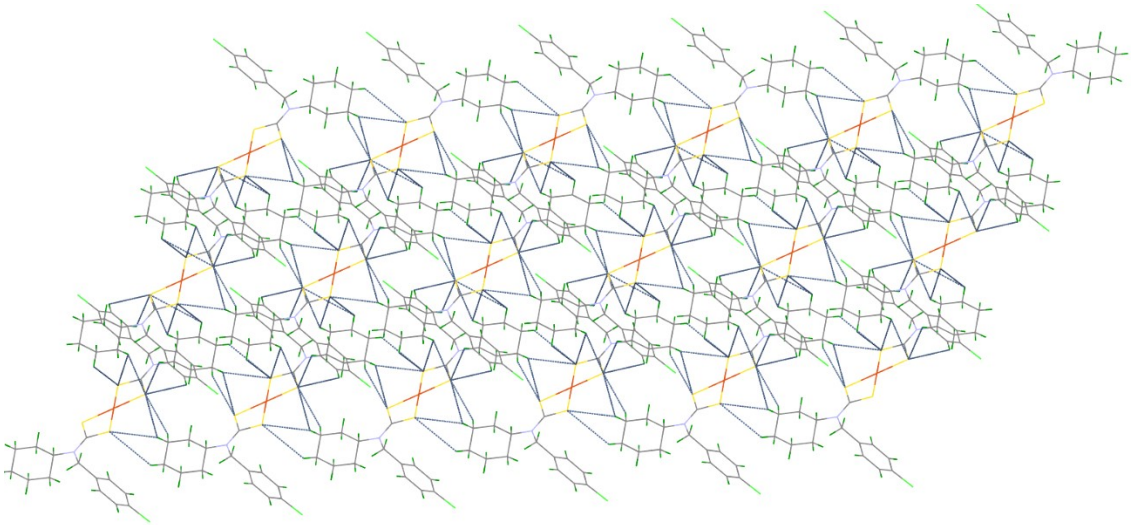

Figure S53. Showing C-H···S hydrogen bonding interactions leading to wave-like architectures in complex **1b**.

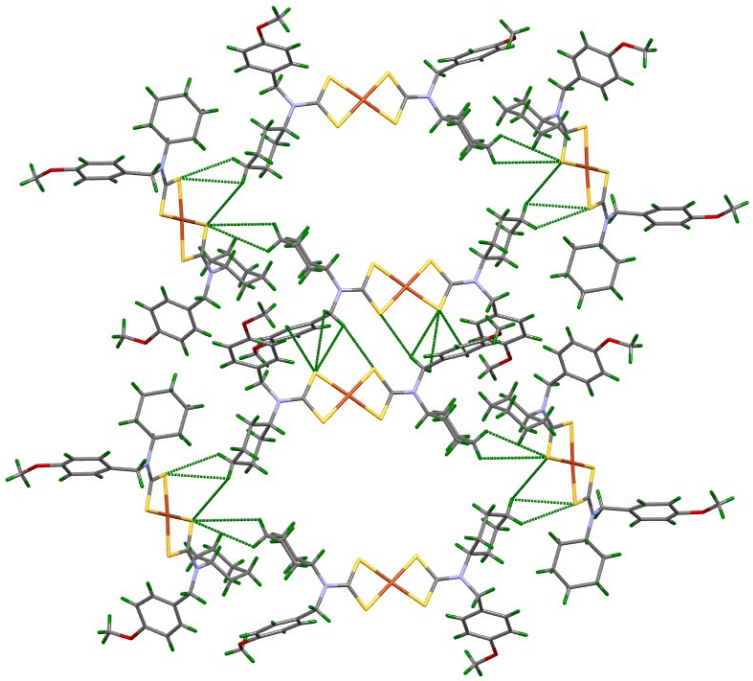

Figure S54. Showing C-H···S hydrogen bonding interactions leading to supramolecular architecture in complex **2b**.

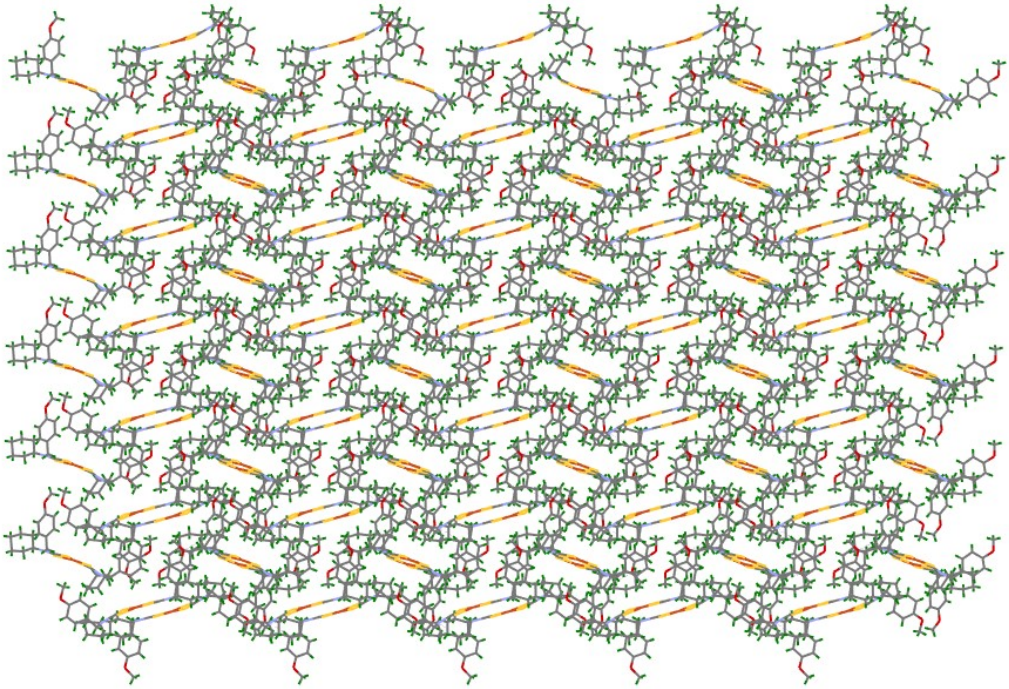

Figure S55. Showing C-H···O hydrogen bonding interactions leading to double helix-like architecture in complex **2b**.

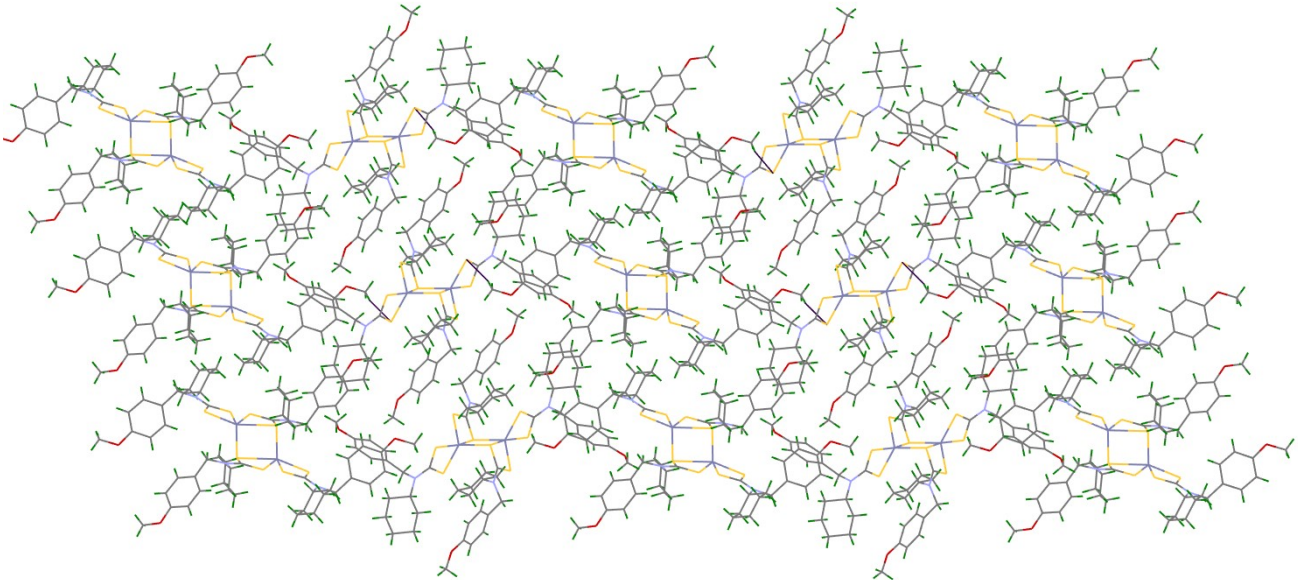

Figure S56. Showing C-H···S hydrogen bonding interactions leading to a ladder-like architecture complex **2c**.

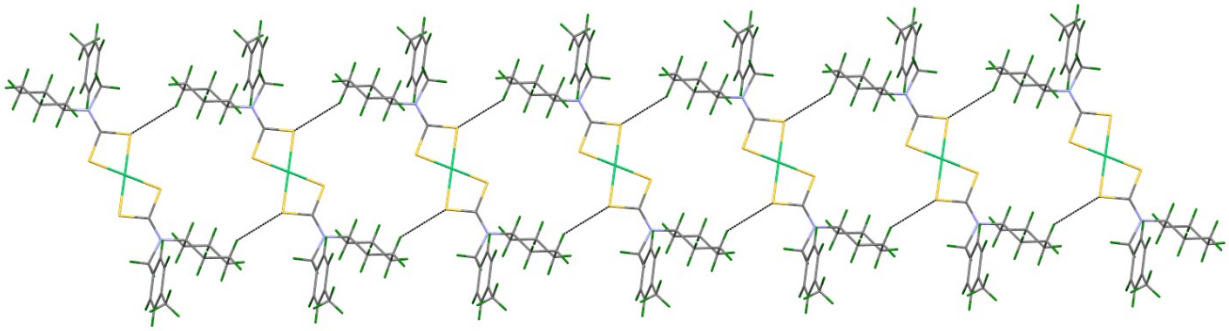

Figure S57. Showing C-H···S hydrogen bonding interactions leading to a linear chain architecture complex **3a**.

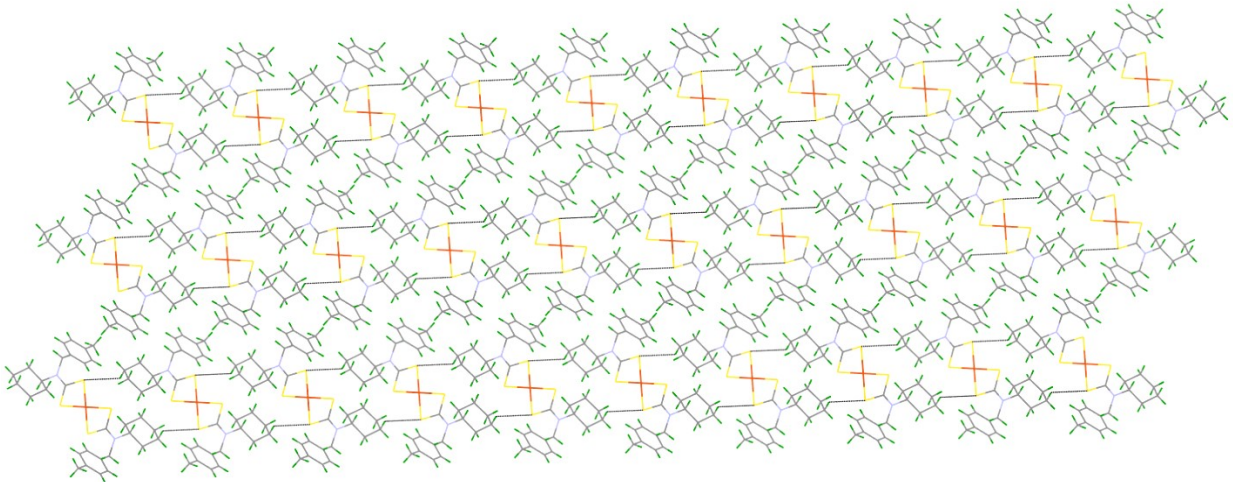

Figure S58. Showing C-H···S hydrogen bonding interactions leading to a swastika-like architecture complex **3b**.

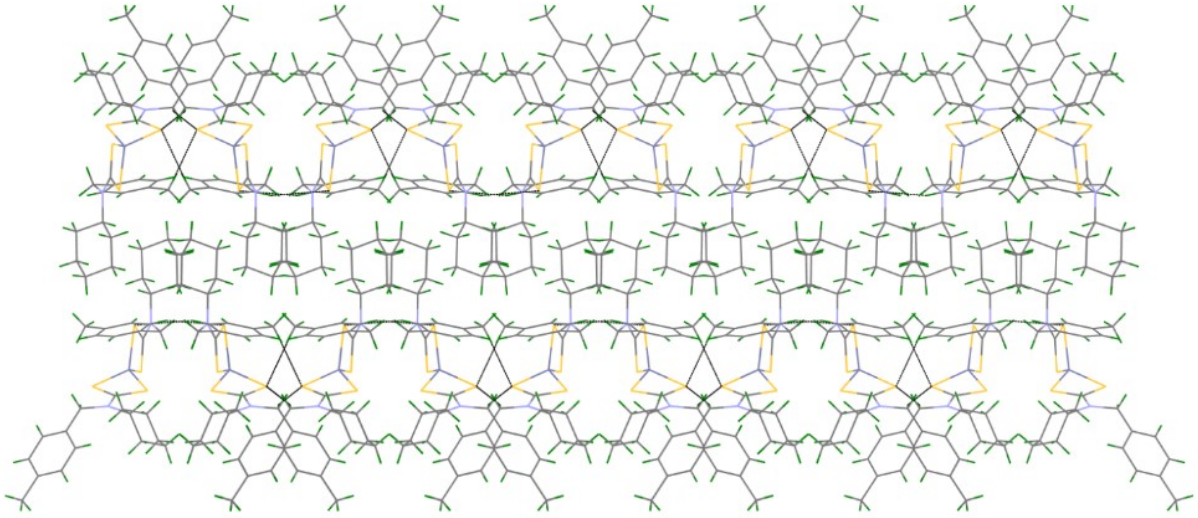

Figure S59. Showing C-H···S hydrogen bonding interactions leading to a wave-like architecture complex **3c**.

7. Biological Application:

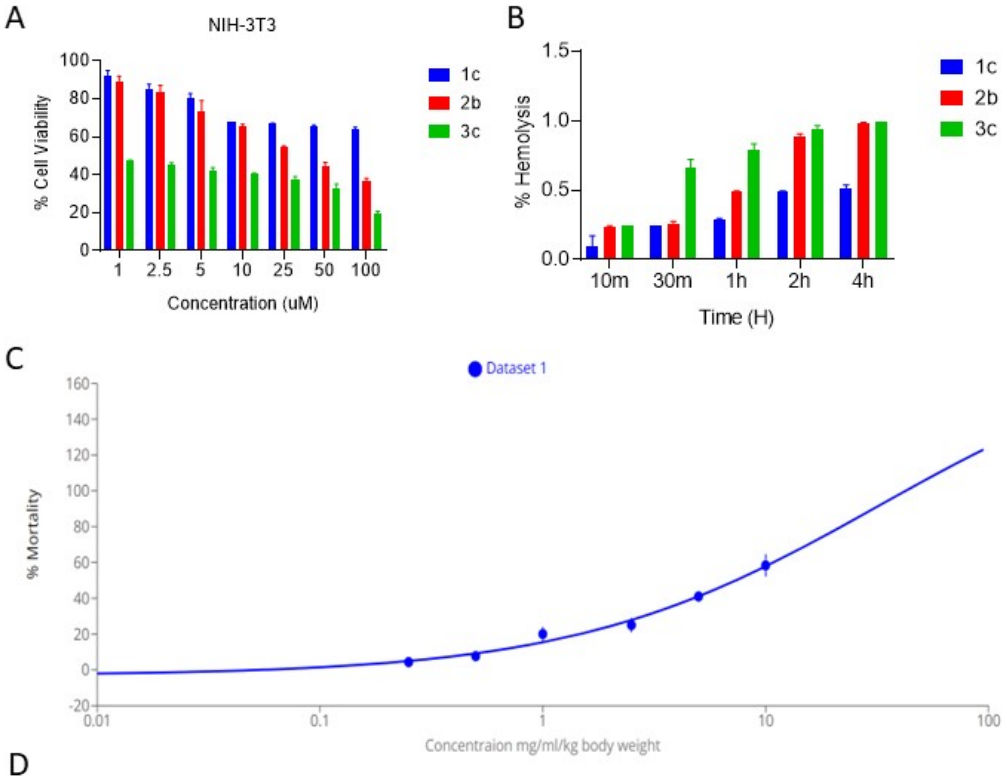

Figure S60. Biosafety Evaluation of Dithiocarbamate Metal Complexes. (A) Viability of normal mouse fibroblast NIH-3T3 cells following treatment with increasing concentrations of metal complexes **1c**, **2b**, and **3c**, as measured by the MTT assay. (B) Hemolysis of red blood cells in response to these metal complexes over time. (C) Probit analysis for the determination of LD_{50} values, used to standardize the dosing for animal studies. Data are presented as mean ± SD of three independent experiments.

8. References:

(1) Sheldrick, G. M. A Short History of *SHELX*. *Acta Crystallogr A* **2008**, *64* (1), 112–122.

(2) Macrae, C. F.; Bruno, I. J.; Chisholm, J. A.; Edgington, P. R.; McCabe, P.; Pidcock, E.; Rodriguez-Monge, L.; Taylor, R.; van de Streek, J.; Wood, P. A. *Mercury CSD 2.0* – New Features for the Visualization and Investigation of Crystal Structures. *J Appl Crystallogr* **2008**, *41* (2), 466–470.

(3) Farrugia, L. J. *WinGX* and *ORTEP for Windows* : An Update. *J Appl Crystallogr* **2012**, *45* (4), 849–854.